

Comparative study of irradiation resistance for multicomponent concentrated HfNbTiZr and dilute V-4Cr-4Ti alloys irradiated with He ions

I.V. Safronov¹, I.A. Ivanov^{2,*}, K. Jin^{3,4,*}, V.V. Uglov^{1,5}, S.V. Zlotski¹, M.M. Belov¹, S. Chen³, Q. Zhang³, A.E. Kurakhmedov², B.S. Amanzhulov², A.E. Ryskulov², A.D. Sapar², A.M. Temir², S.A. Mukhamadiyev², Ye.O. Ungarbayev², G.E. Remnev⁶

1. Belarusian State University, Minsk 220030, Belarus
2. Institute of Nuclear Physics, Almaty 050032, Kazakhstan
3. Department of Materials Science and Engineering, Beijing Institute of Technology, Beijing 100081, China
4. Advance Research Institute of Multidisciplinary Science, Beijing Institute of Technology, Beijing 100081, China
5. National Research Nuclear University MEPhI (Moscow Engineering Physics Institute), Moscow 115409, Russia
6. Tomsk Polytechnic University, Tomsk 634050, Russia

* Corresponding authors. Email addresses: i.ivanov@inp.kz (I.A. Ivanov); jinke@bit.edu.cn (K. Jin).

Keywords: refractory high-entropy alloy, defect energetics, helium-vacancy complex, binding energy, He diffusion, bubble growth.

Abstract

To clarify the efficiency of irradiation resistance, investigation of body-centered cubic concentrated HfNbTiZr and dilute V-4Cr-4Ti alloys, irradiated by 40 keV He ions up to 5×10^{16} , 1×10^{17} and 5×10^{17} cm⁻² fluences at room temperature, was carried out. Similar to V-4Cr-4Ti, HfNbTiZr possesses high phase stability and surface erosion resistance to irradiation with He ions up to 5×10^{17} cm⁻². Using transmission electron microscopy, a more than 2-fold increase in overall swelling, as well as its intensification with increasing fluence was observed for HfNbTiZr compared to V-4Cr-4Ti. Combining atomistic calculations and simulations based on the Modified Embedded Atom Method interatomic potential and Density Functional Theory, the energetics of defects and helium-vacancy complexes, as well as their dynamics, were studied for alloys. It was shown that in the HfNbTiZr and dilute vanadium alloys the number of radiation-induced vacancies (ν) can be comparable. According to the binding energy curves, there is a tendency for higher He accumulation in helium-vacancy complexes due to the increased He/ ν ratio in HfNbTiZr compared to V-4Cr-4Ti (~ 1.5 versus ~ 1.1). It was found that the kick-out of lattice atoms is enhanced in HfNbTiZr and is suppressed in V-4Cr-4Ti. Therefore, the more intense He bubble growth in HfNbTiZr may be due to the kick-out mechanism, which leads to a decrease in the He/ ν ratio and stimulates helium-vacancy complexes to trap additional He atoms. Our results can be used to improve the bubble swelling resistance in the design of new multicomponent concentrated alloys.

1. Introduction

The search for new, in particular, low-swelling materials is necessary for the development of more efficient and reliable fission and fusion reactors [1]. Nuclear reactions occur in the reactor core due to continuous radiation and lead to the accumulation of transmutation gas atoms such as hydrogen and helium. The transmutation gases, along with radiation-induced vacancies, are the origin of the bubble and (or) void nucleation and therefore the cause of material swelling [2]. Currently, one of the promising materials for nuclear applications are single-phase concentrated solid solution alloys, which are also referred to in the literature as multi-principal element alloys, complex concentrated alloys, multicomponent alloys, concentrated multicomponent (multicomponent concentrated) alloys, high-entropy alloys (in the 1st generation sense [3]) [4-6], depending on the emphasized aspect in a particular study. In this paper, the term "multicomponent concentrated alloys" (MCAs) is primarily used.

Numerous studies have shown that MCAs possess, in particular, high thermal creep resistance [7, 8], corrosion resistance [9], as well as radiation resistance [10-20]. By using face-centered cubic (FCC) Ni-containing alloys, it has been demonstrated that radiation damage can be significantly reduced [10-12], as well as void and He bubble formation and irradiation swelling can be suppressed [13-16] by tuning the chemical complexity of MCAs. However, sophisticated composition does not always improve the properties and characteristics of MCAs. For instance, void swelling of three-component NiCoFe and five-component NiCoFeCrMn MCAs is comparable (0.2 *versus* 0.17%, respectively), whereas for a four-component NiCoFeCr alloy, it is higher (0.33%) [14], which is a manifestation of the so-called "cocktail" effect (synergy or emergence, one of the four MCA core effects) [4]. The sophistication of the MCA composition may lead to an enhancement in local lattice distortion (LLD, one of the four MCA core effects) [21], which may be responsible for increased void swelling resistance of NiCoFeCrPd MCAs compared to NiCoFeCrMn [23]. The following mechanisms of increased resistance to void formation in FCC Ni-containing MCAs have been proposed in the literature: i) the mechanism of limited mobility of interstitial clusters and changes in their migration paths, leading to increased recombination of point defects [24]; ii) the chemically biased diffusion and segregation mechanism, which can prevent void growth [25]. At the same time, the positive features of MCAs can be a trigger for enhanced swelling with an increase in the damaging dose at elevated temperatures, as observed for the NiCoFeCr alloy (3 MeV Ni ions, 500 °C, $>8 \times 10^{16} \text{ cm}^{-2}$) [26]. Due to the evolution of the dislocation structure and radiation-induced segregation (RIS), a transition from suppressed to significant void swelling at a dose of more than 86 displacements per atom (dpa) was observed [26]. Nevertheless, by increasing the chemical complexity of MCAs, the degree of RIS can be reduced, as it was found for FCC Ni-containing MCAs (in the sequence NiFe – NiCoFe – NiCoFeCr – NiCoFeCrMn) [27].

Today body-centered cubic (BCC) MCA alloys based on refractory elements are being actively investigated as the most suitable for high-temperature applications [4]. Among them, alloys based on Hf-Nb-Ta-Ti-Zr systems are the most studied [28]. In particular, HfNbTiZr MCA exhibits excellent high-temperature strength and good ductility at room temperature (RT) [29]. However, the issue of radiation resistance of HfNbTiZr is less studied. It has been observed that high-temperature irradiation with He ions (1.5 MeV, 700 °C, 5×10^{15} - $1 \times 10^{17} \text{ cm}^{-2}$) of a single-phase BCC HfNbTiZr alloy led to the formation of hexagonal close-packed (HCP) and FCC nanoprecipitates enriched in Hf and Zr [30]. The latter was the cause of heterogeneous nucleation of He bubbles with a size of tens of nm and at a low density [30]. Similar to FCC Ni-containing MCAs, a relationship between RIS and void swelling can be observed in this case as well [26]. An

increase in the vacancy supersaturation concentration and an intensification of the point defect recombination were proposed as components of the enhanced void swelling resistance at elevated temperatures for BCC NbTiZr MCAs [31]. In addition, NbTiZr demonstrated the absence of RIS and hence phase stability [31].

It is important to emphasize that little attention is paid in the literature to comparing the radiation tolerance of MCAs with reference materials or counterparts. For example, such studies were carried out in Ref. [32] where the radiation resistance of FCC NiCoFeCrMn MCA with austenitic stainless steel AISI-304 (commercial alloy widely used in nuclear power plants [33]) was compared. The formation and growth of He and Xe bubbles in FCC NiFeCrMn MCA and AISI-348 was compared in Ref. [34], and also in Ref. [35] where He bubble formation in BCC TiVTa and TiVNbTa MCAs with the conventional V-4Cr-4Ti alloy (low-swelling alloy for fusion reactor applications [36, 37]) was compared. Previous investigations of helium bubble behavior in refractory MCAs were significantly hampered by irradiation-induced local segregation or precipitates, obscuring the impact of the alloys' intrinsic properties. Therefore, the study of the irradiation swelling resistance of HfNbTiZr in comparison with low-swelling V-4Cr-4Ti is necessary to determine whether the obtained swelling characteristics are outstanding for the MCA. The aim of this work was to conduct a comparative study of radiation resistance for multicomponent HfNbTiZr and V-4Cr-4Ti alloys irradiated with He ions, which fundamentally differ in the doping level (concentrated and dilute solid solutions, respectively).

2. Materials and methods

2.1 Experimental techniques

2.1.1 Preparation of samples

HfNbZrTi and V-4Cr-4Ti bulk alloys were synthesized using the raw pure metals (at least 99.9 wt.%) by induction levitation melting under Ar atmosphere. The as-cast HfNbTiZr ingots were cut into 12 mm thickness slabs, followed by cold rolling to 50 % thickness reduction, then annealed at 1300 °C for 24 h, and water quenched, for achieving homogenized elemental distribution and large grain size according to Ref. 30. The as-cast V-4Cr-4Ti ingots were homogenized at 1100 °C for 12 h according to Ref. 35.

2.1.2 Ion irradiation experiment

The samples were irradiated at a DC-60 heavy ion accelerator at the Astana branch of the Institute of Nuclear Physics (Kazakhstan). Irradiation was carried out with 40 keV He²⁺ ions at fluences of 5×10^{16} , 1×10^{17} and 5×10^{17} cm⁻². Irradiation with helium ions was perpendicular to the surface of the samples. The implantation was performed at a temperature about 300 K (RT). The water cooling of the target substrate was used. To simulate the depth profiles of radiation damage and implanted ions in targets (HfNbTiZr and V-4Cr-4Ti), the SRIM-2013 program [38] was used in the "Full Damage Cascades" mode. To calculate radiation damage in the dpa and the implanted ion concentrations in the at.% we used the method described in [39]. The ranges of 40 keV He ions in both alloys were about 300 nm.

2.1.3 Chemical, structural and microstructural characterizations

The elemental composition in the near-surface layer was analyzed by energy dispersive X-ray spectrometry (EDX) on a JEOL JSM-7500F Field Emission Scanning Electron Microscope.

The results of studying the elemental composition of the HfNbZrTi and V-4Cr-4Ti samples are presented in Table 1. As can be seen from Table 1, the HfNbZrTi alloy is equiatomic with an element concentration of about 25 at.%. The V-4Cr-4Ti alloy is primarily consist of vanadium with about 4 at.% chromium and titanium dopants.

Table 1. Elemental composition of the initial HfNbZrTi and V-4Cr-4Ti alloys.

Alloy	Concentration of elements (at.%)					
	Hf	Nb	Zr	Ti	V	Cr
HfNbZrTi	25.5	25.6	24.0	24.9	-	-
V-4Cr-4Ti	-	-	-	4.7	91.9	3.4

The phase analysis of the samples was carried out by grazing incidence X-ray diffraction (GIXRD) [40] for the study of irradiated regions within the He ion ranges. X-ray patterns were obtained on a Rigaku Ultima IV X-ray diffractometer equipped with a Göbel mirror (parallel beam geometry) and using CuK α characteristic X-ray radiation with a wavelength of $\lambda = 0.154179$ nm. The beam was collimated by slits; the cross section of the X-ray beam behind the slit is 600 mm high and 10 mm wide. GIXRD experiments were performed with the incidence angles of 0.775 and 0.81° for the HfNbTiZr and V-4Cr-4Ti samples, respectively. To exclude the influence of the alloy texture, the experiments were carried out with a constant rotation of the samples at a speed of 30 rps.

Transmission electron microscopy (TEM) and scanning electron microscopy (SEM) analyses were carried out for direct information about the film structure, layer thickness and the sample morphology, respectively. Cross-sectional TEM samples were prepared using a FEI Helios Nanolab 600i focused ion beam (FIB). Trenching and initial thinning the samples were done with 30 keV Ga ions with final polishing at 1 keV ion energy. All samples were analyzed using a FEI Talos F200X transmission electron microscope, operated at 200 kV. For details, see Ref. 35.

2.2 Image software processing

To quantify bubble swelling characteristics from TEM images the ImageJ program [41] was used. For image filtering, the following methods or plugins were mainly used: the Sliding Paraboloid Background Subtraction, the Fast Fourier Transform Bandpass Filter and MorphoLibJ [42]. Bubble swelling (S , %) was evaluated as the ratio of the total volume of all bubbles to the volume of the non-irradiated (region) sample, *i.e.*

$$\sum_i V_{\text{bubble}_i} / \left(V_{\text{post-irrad}} - \sum_i V_{\text{bubble}_i} \right) \times 100, \quad (1)$$

where $V_{\text{bubble}_i} = \pi d_i^3 / 6$; $V_{\text{post-irrad}} = A_{\text{image}} \delta$; d_i is the equivalent (due to asphericity) bubble diameter; A_{image} is the area of the TEM image; δ is the thickness of the irradiated TEM samples, estimated from FIB-SEM observations (about 80-100 nm).

2.3 Simulation techniques

In this paper, the majority of calculations were performed for the HfNbTiZr alloy, while for the relatively well-studied V-4Cr-4Ti alloy and the V-4Ti alloy close to it in composition, the data were taken from the literature.

2.3.1 Generation of initial structures

The initial structures of the HfNbTiZr and V-4Cr-4Ti (V-4Ti) alloys in the form of substitutional solid solutions with BCC lattices were prepared. Supercells with 128 and 240 atoms with a generalized special quasi-random structure model were generated using the USPEX program [43-45]. Supercells with 960, 8192 and 153000 atoms were generated with a random structure model. 3D periodic boundary conditions were used.

2.3.2 Calculations of defect energy characteristics

The calculations of defect energy characteristics were carried out by the molecular statics and dynamics methods using the LAMMPS package [46]. The interatomic interactions for HfNbTiZr were described using the Modified Embedded Atom Method (MEAM) potential [47]. Structural optimization of each defect configuration was performed using a conjugate gradient method with the convergence threshold for forces below 1×10^{-6} eV/Å. The supercell with 240 atoms and the equiatomic composition was used. The formation energy (at 0 K) of vacancies and interstitial atoms was calculated as:

$$E_{def_j}^f = E_{def_j} - E_0 \pm \mu_j. \quad (2)$$

The binding energy of divacancies was defined as:

$$E_{2v}^b = E_{v_j}^f + E_{v_k}^f - E_{2v}^f, \quad (3)$$

where E_{def_j} is the total energy of a relaxed defect structure with a vacancy (v) or an interstitial atom (i) of the j -th atom type; E_0 is the total energy of the variable-cell relaxed ideal structure; μ_j is the chemical potential of the j -th atom type (for v the sign is "+", for i the sign is "-"); $E_{v_j}^f, E_{v_k}^f$ are the formation energies of the considered vacancy j - k pair; E_{2v}^f is the formation energy of the corresponding divacancy. In the calculations, all available lattice sites were taken into consideration. For interstitial atoms, only $\langle 110 \rangle$ and $\langle 111 \rangle$ dumbbell configurations (dumb) were considered due to their lower formation energy for BCC metals [48]. In this case, all possible spatial arrangements of dumbbells, as well as their inversion due to the possible influence of the local chemical environment were taken into account (using the algorithm incorporated in the script).

Taking into account the chemical disorder in the crystal lattice, the calculation of chemical potentials for each atom type was carried out according to the method proposed in [49]. However, in this work, we used the brute-force μ_j averaging method (using the algorithm incorporated in the script) due to the fast calculations of classical atomistic simulation compared to *ab initio* calculations. The calculated μ_j values in the HfNbTiZr alloy were -7.24 ± 0.03 , -7.42 ± 0.05 , -4.84 ± 0.03 and -6.32 ± 0.05 eV for Hf, Nb, Ti and Zr, respectively. While in the pure metals, these values are equal -7.33 , -7.47 , -4.87 and -6.36 eV [47] for the same sequence of elements. Despite the values of μ_j ($j = \text{Nb, Ti, Zr}$) are underestimated compared to the *ab initio* calculations for NbTiZr [31], the obtained data reflect the correct energy trend for the removed or embedded atoms in the system. Chemical potential calculations were carried out on the supercells with 240 and 960 atoms. However, the difference between the average values of μ_j for two supercells turned out to be insignificant (up to the third decimal place).

Migration barriers were calculated using temperature-accelerated dynamics (TAD) [50], implemented in the LAMMPS package, on the supercell with 960 atoms. Since we were interested in collecting statistics in the work, the upper and lower temperatures were set at 873 and 863 K, respectively. Every 0.05 ps, a check was carried out whether a diffusion jump had occurred. A

desired confidence level was set to 90 %, and the minimum pre-exponential factor was equal to 10^{-12} s^{-1} . The system was preliminary equilibrated using a standard timestep of 0.001 ps with the isobaric-isothermal (NPT) ensemble at 873 K; then, the canonical (NVT) ensemble was used. The system was quenched using the standard conjugate gradient minimizer with the force tolerance of $1 \times 10^{-5} \text{ eV/\AA}$. The nudged elastic band (NEB) calculation [51], invoked from TAD, was performed using the "quickmin" damped dynamics minimizer with the standard timestep of 0.001 ps. The force tolerance for NEB calculations was set to $1 \times 10^{-4} \text{ eV/\AA}$. When studying dumbbell diffusion, after the simulation was completed, an algorithm was used to extract migration barriers and jumping atoms.

2.3.3 Collision cascade simulations

To simulate atomic collision cascades the molecular dynamics (MD) method with LAMMPS was used. Note that according to the SRIM simulations of 40 keV He ion collision cascades in the HfNbTiZr and V-4Cr-4Ti targets, the probability of energy transfer above 500 eV to primary knock-on atoms (PKAs) is about 8-9 %, while the "average" energy of PKAs in such events is about 1 keV. Considering the low efficiency of radiation damage for PKAs with energies of several hundred eV, the MD simulations of collision cascades were performed at a PKA energy of 1 keV and 300 K using a supercell of $30 \times 30 \times 85$ unit cells (153000 atoms). HfNbTiZr was considered with the equiatomic composition, and V-4Ti consisted about 4.3 at.% Ti. For HfNbTiZr and V-4Ti, the MEAM interatomic potentials [47] and [52] were used, respectively, taking into account the Ziegler-Biersack-Littmark (ZBL) repulsive potential [53] at short distances. The available interatomic potential for the V-Ti solid solutions correctly describes, in particular, many energy characteristics of defects and their complexes [52].

The structures were preliminary optimized with a variable cell and then were equilibrated with the NPT ensemble at 300 K for 100 ps. A PKA was randomly selected in the supercell. Almost the entire velocity along the largest supercell size was transferred to a PKA. To describe the collisional and recombination stages of cascade evolution, an adaptive timestep was used so that any atom did not move more than 0.02 Å in one-step. Simulations of these stages were performed using the microcanonical (NVE) ensemble approximately up to 1 ps, the further so-called thermalization stage was simulated using the NPT ensemble during 50 ps at 300 K. To obtain an average evaluation of the number of surviving Frenkel pairs, 20 tests were carried out for each alloy.

2.3.4 Calculations of binding energy for helium-vacancy complexes, simulations of helium diffusion and evolution of helium-vacancy complexes

Due to the lack of reliable interatomic potentials to describe the He behavior in the HfNbTiZr and V-4Cr-4Ti alloys, the binding energy calculations of helium-vacancy complexes ($\text{He}_{n\nu m}$) and helium diffusion simulations were performed based on the density functional theory (DFT) and the plane-wave pseudopotential approach as implemented in the Quantum ESPRESSO package [54-56]. The generalized gradient approximation (GGA) with the Perdew-Burke-Ernzerhof (PBE) functional [57] for the exchange–correlation interaction and the semi-core projector-augmented wave (PAW) method [58, 59] for the ion–electron interaction were applied. For He-He and He-metal interactions, Van der Waals interactions were neglected (the effect is quite small [60]). The Marzari-Vanderbilt-DeVita-Payne smearing [61] with a $7.35 \times 10^{-3} \text{ Ry}$ spreading was employed. The kinetic energy cutoff for wave functions was set to 60 Ry. For the mixing mode, local-density-dependent Thomas-Fermi screening was used. The $4 \times 4 \times 4$ supercell containing 128 atoms ($\text{Hf}_{32}\text{Nb}_{32}\text{Ti}_{32}\text{Zr}_{32}$ and $\text{V}_{118}\text{Cr}_4\text{Ti}_6$) was used and the Brillouin zone was

sampled with a $3 \times 3 \times 3$ k-point mesh generated in the Monkhorst-Pack scheme [62]. The convergence threshold for the total energy and forces were 7.35×10^{-5} Ry and 3.889×10^{-4} Ry/Bohr, respectively. For the initial structure and subsequent structures with $\text{He}_n\nu_m$ complexes, optimization at a variable cell and a constant cell was performed, respectively.

$\text{He}_n\nu_m$ complexes were generated using the AtomsK program [63]. The binding energy of $\text{He}_n\nu_m$ complexes (0 K) was calculated using the formulas [64, 65]:

for ν to $\text{He}_n\nu_{m-1}$

$$E_{\nu-\text{He}_n\nu_{m-1}}^b = E_\nu + E_{\text{He}_n\nu_{m-1}} - E_{\text{He}_n\nu_m} - E_0, \quad (4)$$

for He to $\text{He}_{n-1}\nu_m$

$$E_{\text{He}-\text{He}_{n-1}\nu_m}^b = E_{\text{He}} + E_{\text{He}_{n-1}\nu_m} - E_{\text{He}_n\nu_m} - E_0, \quad (5)$$

where E_ν , E_{He} and $E_{\text{He}_n\nu_m}$ are the total energies of a relaxed defect structure with a vacancy, with a tetrahedral (low formation energy in BCC metals and alloys [60, 66-69]) interstitial He atom and with a $\text{He}_n\nu_m$ complex consisting of n He atoms ($n = 1, 2, 3$) and m vacancies ($m = 1, 2, 3$), respectively. The most stable $\text{He}_n\nu_m$ configurations were taken from Refs. [64, 65], found for V and Ta.

The helium diffusion simulations were studied by the *ab initio* (Born-Oppenheimer) molecular dynamics (AIMD), implemented in Quantum ESPRESSO. A single k-point was used for the $4 \times 4 \times 4$ supercell. Initially, the structures with a tetrahedral He atom were equilibrated with variable-cell AIMD during 4 ps to account for thermal expansion, and then constant-cell AIMD was used for about 12 ps with a timestep of 2 fs. The ion temperature was controlled *via* the "rescaling" option and the Berendsen thermostat for variable-cell AIMD and constant-cell AIMD, respectively. To accelerate the He diffusion, the temperature was set to 1173 K. After the simulations were completed, the mean square displacement (MSD) for He, averaged over 3 independent trajectories, was calculated using the meanSquaredDisplacement code [70].

Simulations of the evolution for helium-vacancy complexes were performed using variable-cell AIMD at 300 K for about 4-12 ps. For this purpose, $\text{He}_9\nu$, $\text{He}_{11}\nu$, $\text{He}_{13}\nu$ and $\text{He}_{15}\nu$ complexes with the increased He/ ν ratio (9, 11, 13 and 15, respectively) were considered. The structures with these complexes were preliminary optimized at a variable cell.

2.3.5 Visualization and analysis of structures

The analysis and visualization of the structures were carried out using the OVITO software [71]. The Wigner-Seitz cell method and the dislocation extraction algorithm, implemented in OVITO, were used to analyze the point defects and dislocation structures, respectively. Atomic volumes were calculated in OVITO based on the Voronoi tessellation algorithm. To analyze the influence of the local chemical environment on the defect energy characteristics, partial coordination numbers were calculated using LAMMPS.

3. Results

3.1 Experiment

3.1.1 XRD analysis

The results of studying the phase composition of the initial and irradiated by He ions samples of HfNbTiZr and V-4Cr-4Ti are shown in Figure 1. GIXRD patterns were obtained at

grazing incidence angles of 0.775 and 0.81° for HfNbZrTi and V-4Cr-4Ti, respectively. These angles correspond to the X-ray penetration depth comparable to the He ion ranges of about 300 nm.

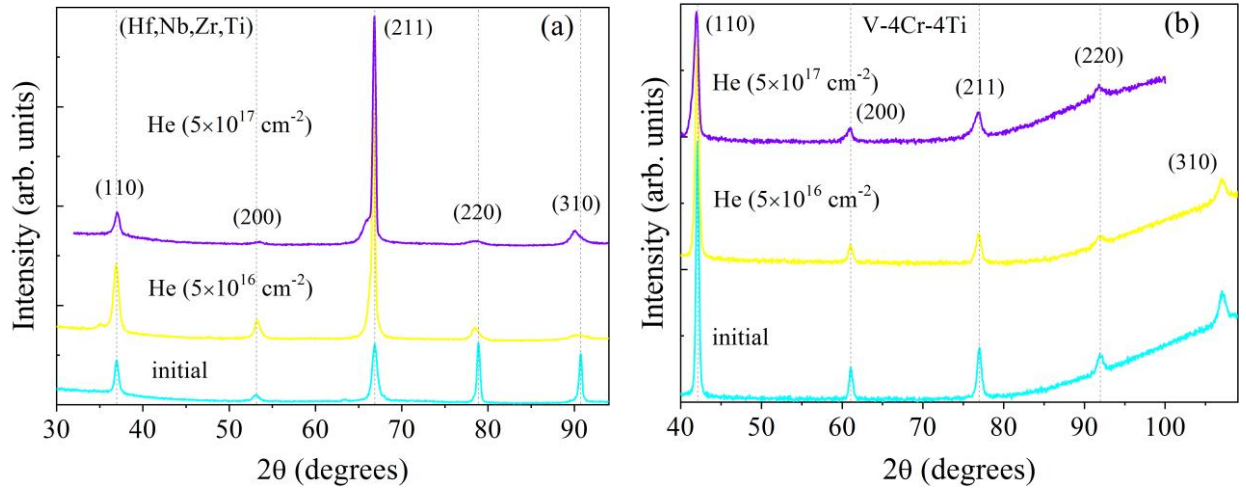


Fig. 1. GIXRD patterns of the initial and irradiated by 40 keV He^{2+} ions at RT up to $5 \times 10^{17} \text{ cm}^{-2}$ (a) HfNbZrTi and (b) V-4Cr-4Ti samples.

The analysis of the formed phases in the HfNbTiZr samples showed that all diffraction peaks are identified to belonging to a single-phase BCC structure in the form of substitutional solid solution. The V-4Cr-4Ti samples represent the BCC V phase with substitutional solute Ti and Cr atoms. Calculated from the GIXRD patterns with Integrated Powder X-ray Diffraction PDXL2 Software, the lattice constants were 3.4309 ± 0.0003 and $3.03025 \pm 0.0004 \text{ \AA}$ for HfNbZrTi and V-4Cr-4Ti, respectively.

The GIXRD pattern analysis of the alloys did not reveal the formation of new phases or decomposition of the solid solution phases, which indicates high resistance of the alloy phase compositions to irradiation with 40 keV He ions at RT up to a fluence of $5 \times 10^{17} \text{ cm}^{-2}$. A slight shift of the phase diffraction lines towards smaller 2θ (Fig.1) was observed. It indicates an increase in the lattice constant of HfNbTiZr and V-4Cr-4Ti, which is associated with the accumulation of radiation-induced defects and an increase in the density of helium-vacancy clusters. With an increase in fluence to $5 \times 10^{17} \text{ cm}^{-2}$ the lattice constant increases by 0.35 % and 0.17 % for HfNbTiZr and V-4Cr-4Ti, respectively.

3.1.2 TEM analysis and image processing

Figure 2 shows the ion range distributions of He bubbles in the HfNbTiZr and V-4Cr-4Ti alloys, irradiated at RT with fluences of 1×10^{17} and $5 \times 10^{17} \text{ cm}^{-2}$. The concentration and radiation damage profiles obtained from SRIM (theoretical values of the He concentration and radiation damage increase by 5 times at $5 \times 10^{17} \text{ cm}^{-2}$ relative to those at $1 \times 10^{17} \text{ cm}^{-2}$) are consistent with the spatial distribution of He bubbles in the TEM images (Fig. 2). It was observed larger He bubbles formed in the HfNbTiZr alloy than in V-4Cr-4Ti (clearly fixed at the fluence of $5 \times 10^{17} \text{ cm}^{-2}$). However, even at the fluence of $5 \times 10^{17} \text{ cm}^{-2}$ (the damaging dose is about 25 dpa), the formation of He bubbles larger than 10 nm (Fig. 2(c)) in the HfNbTiZr alloy was not observed in the case of irradiation at RT.

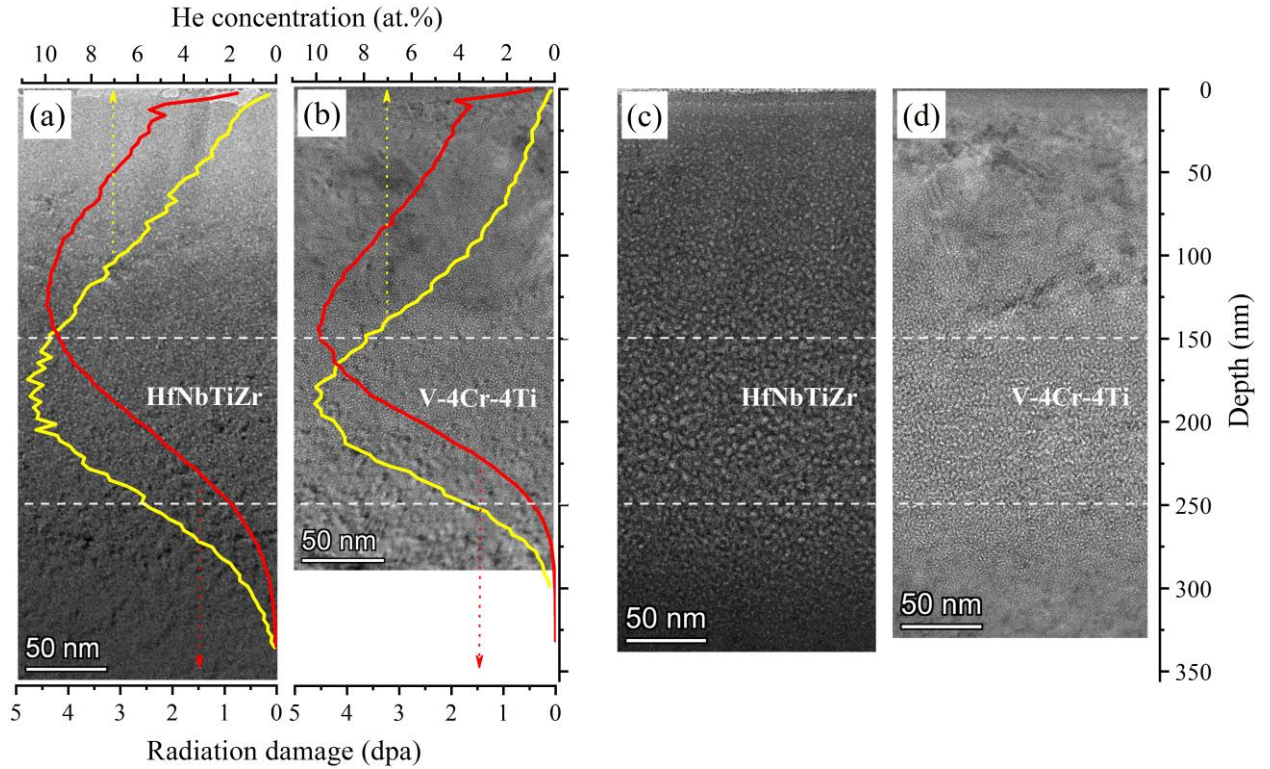


Fig. 2. Under-focused TEM bright field images in the ion ranges of the HfNbTiZr and V-4Cr-4Ti alloys, irradiated by 40 keV He⁺² at RT up to (a), (b) 1×10^{17} and (c), (d) 5×10^{17} cm⁻². The SRIM He concentration and radiation damage profiles in the alloys correspond to the fluence of 1×10^{17} cm⁻².

The interval of 150–250 nm, marked in Fig. 2, corresponds to the peak region of He bubbles. In higher resolution, this region is shown for both alloys in Figures S1 and S2 (see the Supplementary Material) for the fluences of 1×10^{17} and 5×10^{17} cm⁻², respectively. Despite the close occurrence depths of implanted He relative to the surface of HfNbTiZr and V-4Cr-4Ti, SEM studies of the surface microstructure of the alloys showed the absence of blisters and exfoliation at the fluence of 5×10^{17} cm⁻² (see Fig. S3 in the Supplementary Material).

¶It was defined that the HfNbTiZr alloy has a 2 times wider size distribution of He bubbles than for V-4Cr-4Ti, while the equivalent diameters were 1.3 ± 0.5 versus 0.7 ± 0.2 nm and 3.1 ± 1.1 versus 1.4 ± 0.6 nm at the fluences of 1×10^{17} and 5×10^{17} cm⁻², respectively (Figs. 3(a) and 3(b)). Hence, both alloys are characterized by a finely dispersed bubble structure, which is a consequence of their increased resistance to bubble swelling compared to pure BCC metals, e.g. vanadium [72]. Nevertheless, the HfNbTiZr alloy is more susceptible to bubble swelling than V-4Cr-4Ti (Figs. 3(c) and 3(d)). The overall swelling (S_{overall} , according to the ion range depths) for the HfNbTiZr and V-4Cr-4Ti alloys was 0.10 ± 0.01 versus 0.056 ± 0.006 % and 0.44 ± 0.05 versus 0.19 ± 0.02 % at the fluences of 1×10^{17} and 5×10^{17} cm⁻², respectively (Fig. 3(c)). Thus, a 5-fold increase in the fluence (from 1×10^{17} to 5×10^{17} cm⁻²) led to a 3.5-fold increase in S_{overall} for the V-4Cr-4Ti alloy, for the HfNbTiZr alloy this is already a 4.4-fold increase. The peak bubble swelling is 3 times greater than the overall swelling for both alloys (Figs. 3(c) and 3(d)), while for the highest fluence it was 1.4 ± 0.2 and 0.59 ± 0.07 % for the HfNbTiZr and V-4Cr-4Ti alloys (Fig. 3(d)), respectively. Along with this, the overall density of He bubbles in the HfNbTiZr alloy was 2.1 and 2.5 times lower than in V-4Cr-4Ti at the fluences of 1×10^{17} and 5×10^{17} cm⁻², respectively (Fig. 3(e)). While for V-4Cr-4Ti, the dose dependence shows a 2.4-fold decrease in peak bubble density with increasing fluence, for HfNbTiZr, there is already a 3-fold decrease (Fig. 3(f)). Thus, the above

results also indicate an intensification of bubble swelling in the HfNbTiZr alloy compared to V-4Cr-4Ti with an increase in fluence.

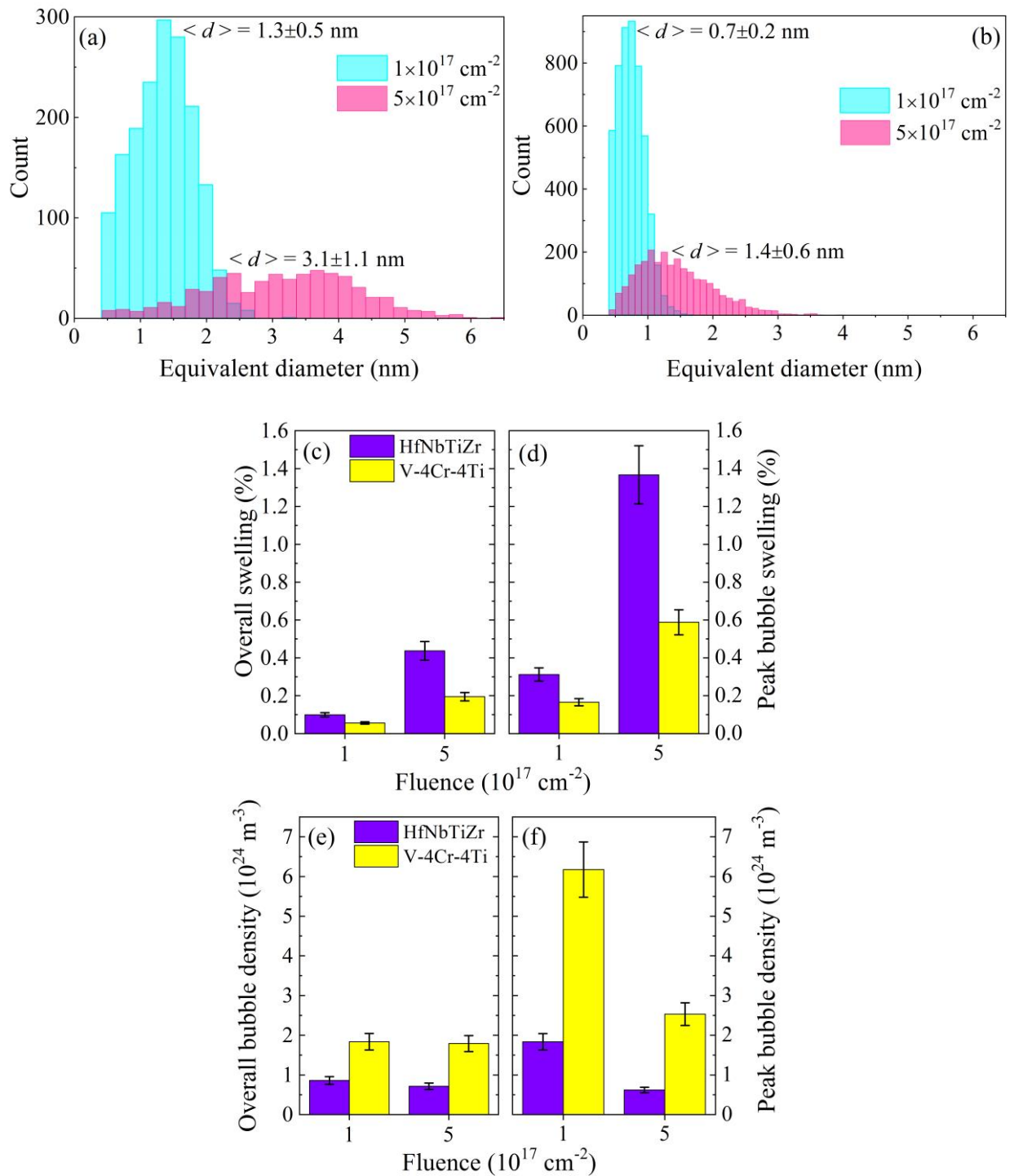


Fig. 3. Bubble swelling characteristics (40 keV He ions, RT): the bubble size distributions in (a) HfNbTiZr and (b) V-4Cr-4Ti; the histograms of (c) overall, (d) peak bubble swelling and of (e) overall, (f) peak bubble density for both alloys.

A number of experimental works indicate a high resistance to radiation damage and swelling of the V-4Cr-4Ti alloy [35-37, 72-74]. The evaluation of the bubble swelling characteristics for the V-4Cr-4Ti alloy does not contradict the data [72, 74], according to which either no visible He bubbles were observed in the alloy (50 keV, RT, $5 \times 10^{16} \text{ cm}^{-2}$ [74]), or the

average He bubble diameter was 1 nm with $S_{\text{overall}} = 0.21 \pm 0.05 \%$ (40 keV, 650 °C, $5 \times 10^{16} \text{ cm}^{-2}$ [72]).

3.2 Simulation

Considering that the nature of radiation damage in reactor materials is mainly determined by the formation, distribution and interaction of 0D, 1D, 2D and 3D radiation-induced defects [75], the primary task is to study the energy characteristics of point defects and their complexes, which are the origin in the evolution of a particular defect structure.

3.2.1 Formation energy of vacancies and interstitial atoms

The vacancy formation energy (E_v^f) for HfNbTiZr in comparison with V-4Cr-4Ti and reference metals are provided in Fig. 4. It was found the HfNbTiZr alloy has an inherent decrease in the formation energy for all vacancy types compared to the reference BCC Nb (2.68 eV), while the average values are close to 1.6 eV (Fig. 4). Among Hf, Nb, Ti and Zr, only Nb has the main BCC phase, and the remaining elements have the stable low-temperature HCP (α) phase [76]. At the same time, the V-4Cr-4Ti alloy [77] is characterized mainly by the reverse trend (Fig. 4): the formation energy of νV and νCr vacancies is greater than in the reference BCC V (as the solvent). Note the E_v^f distributions were obtained only for the solvent atoms of the V-4Ti alloy [78]. With that, the average E_v^f values for the V-4Ti alloy were 1.6 and 2.1 eV for the Ti-bind νV and isolated νV vacancy [78], respectively (not shown in Fig.). The latter value actually coincides with that for the reference V [77, 79, 80]. Considering the low concentration of the Ti dopant (about 4 at.%), the comparability of the E_v^f values in the V-4Ti alloy and the reference metal (see Fig. 1 from [78]) is assumed (weighted average E_v^f is about 2.0 eV), in contrast to the HfNbTiZr alloy. Thus, the data of vacancy formation energies show the ease of vacancy formation in the concentrated HfNbTiZr alloy compared to the dilute V-4Cr-4Ti [77] and V-4Ti [78] alloys. Taking into account the lower formation energies of vacancies in the HfNbTiZr alloy, their equilibrium concentration (C_v^0) will be higher than in V-4Cr-4Ti and V-4Ti. The almost full overlap of E_v^f distributions in the HfNbTiZr alloy (Fig. 4) suggests the equiprobability of all-type formation of vacancies, while the V-4Cr-4Ti and V-4Ti alloys tend to prefer the formation of νTi vacancies and Ti- νV (solute – solvent vacancy) complexes [77, 78, 81].

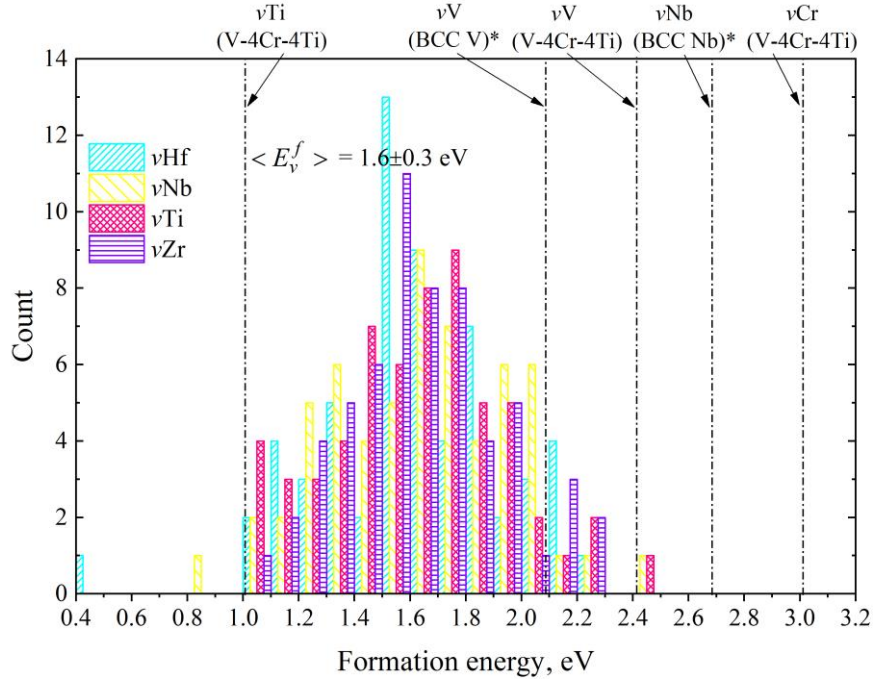


Fig. 4. Formation energy of vacancies for the HfNbTiZr alloy. For comparison, the data for the reference Nb and V [79, 80], as well as V-4Cr-4Ti [77] are given. "*" mean averaging according to the data [79, 80].

As noted in Ref. [31], the lower E_v^f in the NbTiZr alloy compared to its constituent elements can be attributed to the significant overall structural relaxation around a vacancy (promotes the rearrangement into the lowest energy atomic configuration), which is a consequence of severe LLD and dependence on the local chemical environment. The results of our calculations, based on the MEAM interatomic potential [47], show the same trend for HfNbTiZr. Earlier, *ab initio* calculations showed that the average atomic displacements (Δd as a degree of LLD) in BCC HfNbTiZr is more than 3 times higher than in FCC NiCoFeCr [21]. Note the underestimation of Δd values for HfNbTiZr calculated with the MEAM potential compared to the *ab initio* calculations [21] (0.08 *versus* 0.20 Å, respectively). It is also necessary to mention the influence of the "cocktail" effect in MCAs [4]. For example, for FCC NiCoCr and NiCoFeCr, all E_v^f values were higher than in the reference FCC Ni [82], while in the BCC VTaCrW, most of the E_v^f values turned out to be higher than in the reference BCC V, Cr, Ta, but lower than in W [83].

Figure 5 demonstrates the influence of the above-mentioned effects of structural relaxation and local chemical environment [31] on E_v^f for the HfNbTiZr alloy. The Δd values in HfNbTiZr after variable-cell structural optimization with a vacancy clearly prove their preponderance compared to Nb (Fig. 5(a)). A strong correlation between E_v^f and Δd for the alloy is not observed (Fig. 5(a)) due to the local chemical environment effect (Fig. 5(b)). In the first nearest neighbor (1NN) shell, Nb and Zr atoms provide a crucial and contrary effect on E_v^f : an increase in the Nb fraction contributes to an increase in E_v^f , while an increase in the Zr fraction leads to a decrease in E_v^f (Fig. 5(b)). Previously, *ab initio* calculations for the NbTiZr alloy [31] showed a decrease in the Nb fraction in the 1NN shell leads to larger structural relaxation and, as a consequence, to a decrease in E_v^f . There is also a trend where an increase in any species fraction contributes to a

decrease in the spread of E_v^f values (Fig. 5(b)). A weak correlation between the size of the atom being removed during vacancy creation (Fig. 5(c)) and Δd (Fig. 5(a)) was also shown for other BCC MCAs [31, 83].

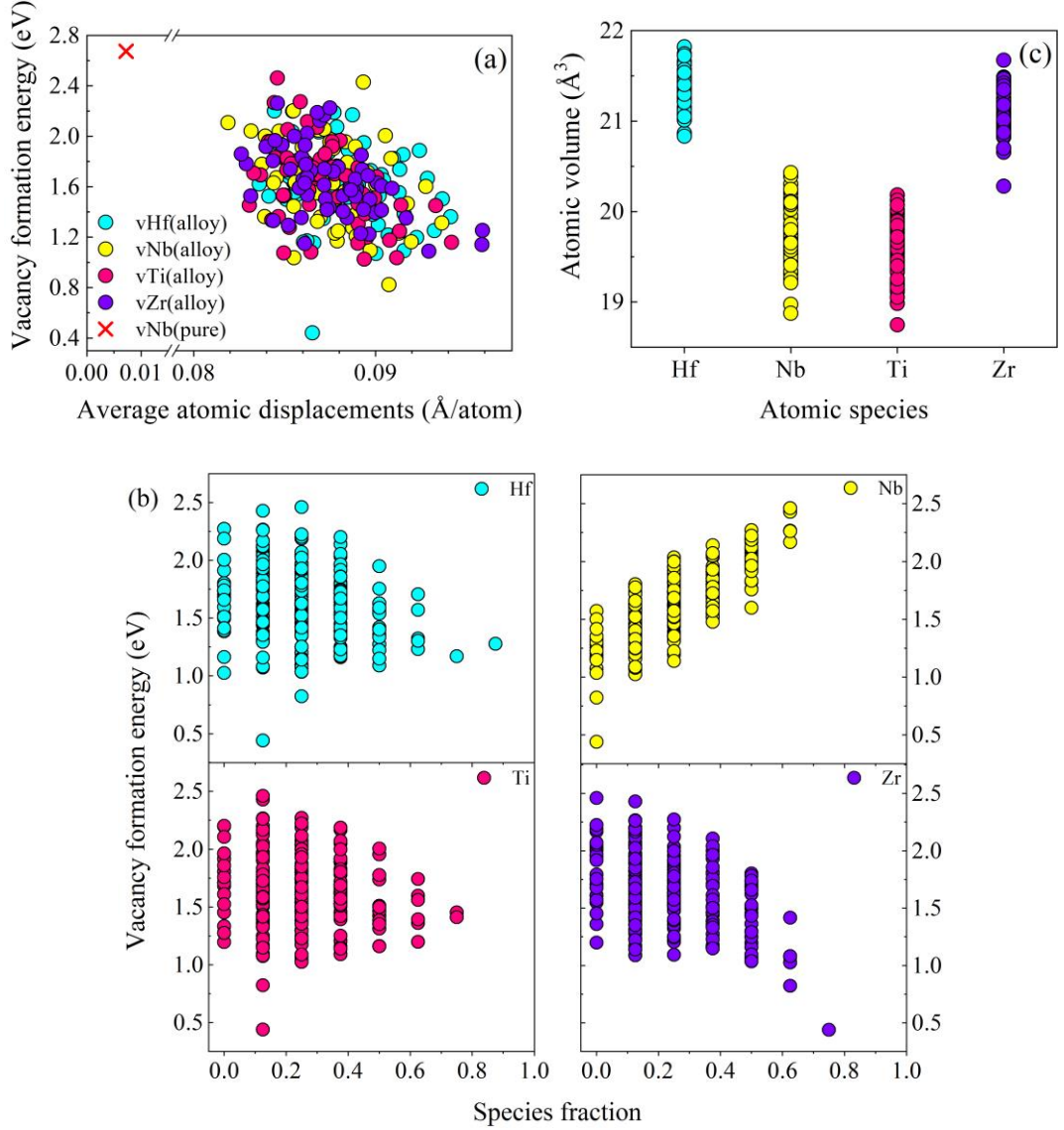


Fig. 5. The effect of (a) overall structural relaxation and (b) local chemical environment in the 1NN shell on E_v^f , as well as (c) the atomic volume distribution in the HfNbTiZr alloy.

It is known that in BCC metals $\langle 111 \rangle$ interstitial configurations (dumbbell and crowdion) have lower formation energies compared to $\langle 110 \rangle$ dumbbells and other configurations, except for Cr and Fe [80]. The calculations showed in the HfNbTiZr alloy $\langle 110 \rangle$ dumbbells are more stable than $\langle 111 \rangle$ dumbbells. A similar trend was observed in the NbTiZr alloy, where for half of the dumbbell types (for pairs Nb-Ti, Ti-Ti, Zr-Ti) $\langle 110 \rangle$ dumbbells had a much higher occurrence probability than $\langle 111 \rangle$ dumbbells [31]. Similarly, in the VTaCrW alloy, only 20 % of the dumbbells were oriented in the $\langle 111 \rangle$ direction [83]. Therefore, the basic calculations of the interstitial atom formation energy (E_i^f) for the HfNbTiZr alloy were carried out for the $\langle 110 \rangle$ dumbbell configuration.

Figure 6 displays that the HfNbTiZr alloy is characterized by a separation of interstitial pairs into two approximately equal parts: easy and hard formed dumbbells compared to the reference Nb (4.18 eV). The lowest average E_i^f values for different pairs are close to 3.2 eV. Ti-

Ti, Nb-Nb, Nb-Ti, Hf-Ti and Ti-Zr dumbbells are easy formed, while Zr-Zr, Hf-Hf, Hf-Zr, Hf-Nb and Nb-Zr dumbbells are hard formed. According to available literature data for the V-4Ti alloy, the crowdion formation energy decreases near Ti atoms due to the release of energy during the formation of Ti-*i*V, 2Ti-*i*V, *etc.* binding states (down from 2.8 to 2.2 eV for crowdion and 3Ti-*i*V complex, respectively) [78]. Similarly, as for vacancies, it can be assumed that the E_i^f values in the V-4Ti alloy and reference V are comparable (see Fig. 1 from [78]). This means that most of the E_i^f values from the distribution in the V-4Ti alloy (weighted average E_i^f is about 2.7 eV) are lower than the lowest average E_i^f (3.2 eV) for the HfNbTiZr alloy (Fig. 6). Therefore, it is expected that in the concentrated HfNbTiZr alloy, the formation of interstitial atoms is more difficult than in the dilute V-4Ti and V-4Cr-4Ti alloys.

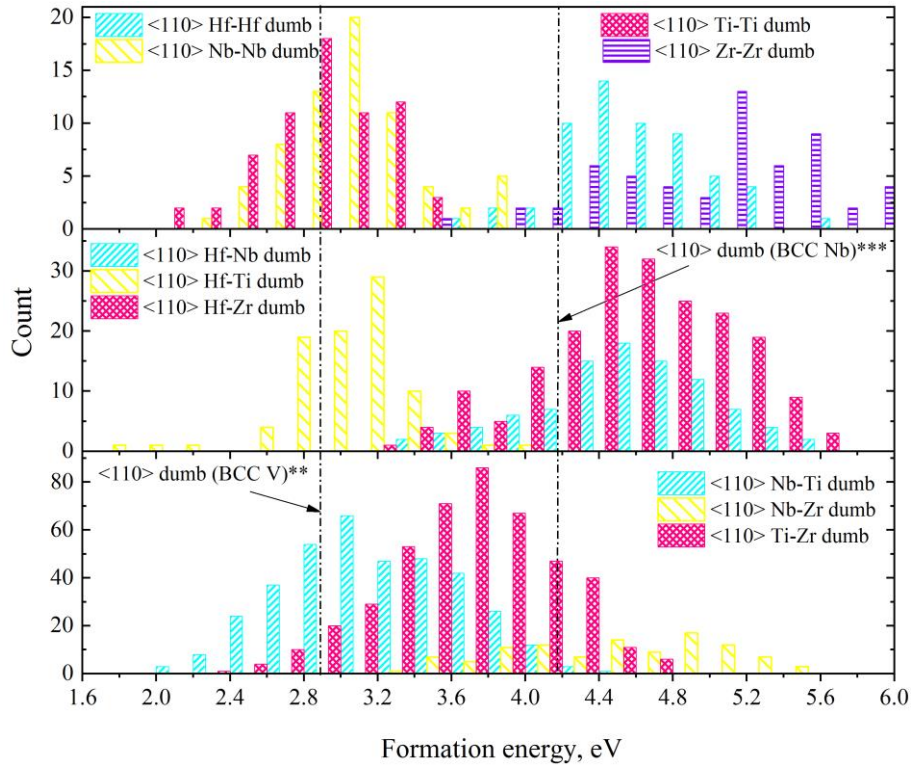


Fig. 6. Formation energy of <110> dumbbells for the HfNbTiZr alloy. For comparison, the data for the reference Nb [80, 84] and V [78, 80] are given. "***" and "**" mean averaging according to the data [78, 80] and [80, 84], respectively.

The decrease in the formation energy of Ti-Ti, Nb-Nb, Nb-Ti, Hf-Ti and Ti-Zr dumbbells for the HfNbTiZr alloy compared to the reference Nb is a consequence of the increased binding interaction between a certain pair of interstitial atom – lattice atom [13] similarly to the V-4Ti alloy [78]. The observed trend in the preferential formation for most dumbbell pairs for HfNbTiZr is consistent with the data of *ab initio* calculations for the NbTiZr alloy [31]. In addition, the decrease of E_i^f in the HfNbTiZr alloy compared to the reference metal is consistent with the data for other MCAs with FCC [82] and BCC [83] lattices.

3.2.2 Divacancy binding energy

The divacancy binding energy (E_{2v}^b) affects the early stage of vacancy clustering (*e.g.* [79]), and thus the void and bubble swellings as well. Its positive value corresponds to the

attraction, while its negative value corresponds to the repulsion of vacancies. Figure 7 displays the E_{2v}^b distributions for the HfNbTiZr alloy compared to Nb, as well as for V (dashdotted lines). It is defined the HfNbTiZr alloy is characterized by the same divacancy configurations in terms of the stability as for the reference Nb. That is, vacancies in the second nearest neighbor (2NN) shell form a stable configuration (Fig. 7), and in the 1NN shell form a metastable configuration (see Fig. S4 in the Supplementary Material) [79]. From Fig. 7 it follows that most of the E_{2v}^b values for HfNbTiZr lie to the left of "2v (BCC Nb)". This means that divacancies in the HfNbTiZr alloy are much less stable than in Nb (0.56 and 0.38 eV for the stable and metastable divacancy in Figs. 7 and S4, respectively). For most 2NN divacancy configurations, the average E_{2v}^b values are below 0.1 eV. In turn, the V-4Cr-4Ti alloy is characterized by high binding energies for the Ti-vV complexes: 0.61 eV for Ti-vV, 0.95 eV for Ti-2vV, 1.22 eV for 2Ti-vV, 1.17 eV for 3Ti-vV [81]. However, in the case of attachment the second vV vacancy to the Ti-vV complex, the energy gain is 0.34 eV, which is lower by 30 % than E_{2v}^b of a pure 2vV divacancy (0.45 eV) [81]. Therefore, it is energetically favorable for multiple solute – solvent vacancy complexes to form rather than solute – solvent divacancy [81].

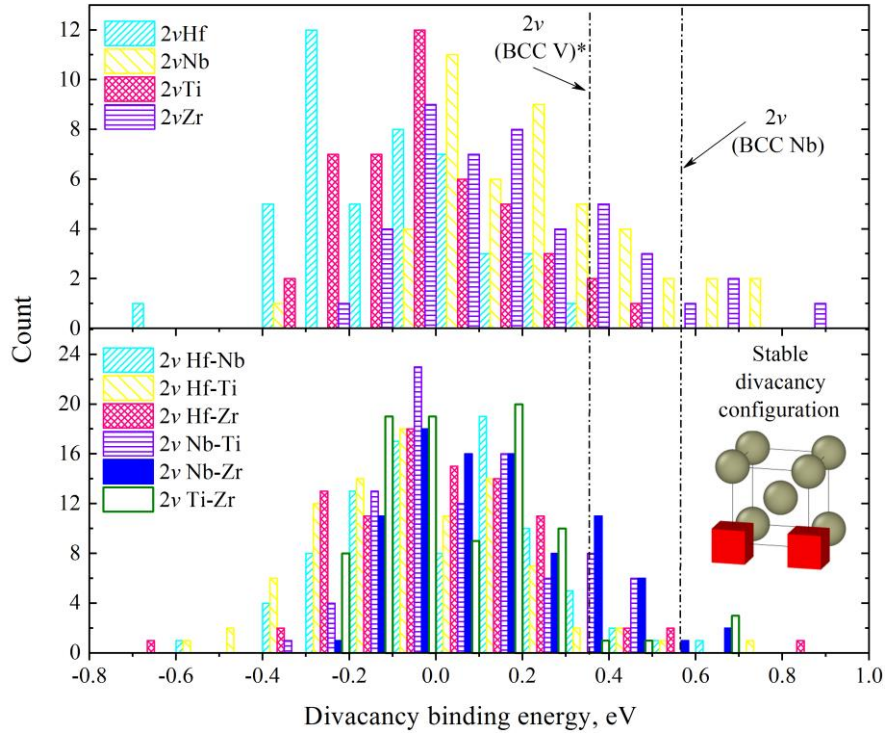


Fig. 7. Divacancy binding energy for stable configurations in the HfNbTiZr alloy. For comparison, the data for the reference Nb [79] and V [79, 81] are given (dashdotted lines). "*" means averaging according to the data [79, 81].

The E_{2v}^b data for the concentrated HfNbTiZr and dilute V-4Cr-4Ti, V-4Ti alloys [78, 81], indicate hindered clustering of vacancies compared to the reference Nb and V, respectively. Indeed, MD annealing (supercell with 8192 atoms) at 873 K for 15 ns of several HfNbTiZr alloy samples with 2.5 % vacancy concentration [85, 86] confirmed that a vacancy ensemble does not transform into large clusters (Fig. 8(a)). In contrast, in the reference Nb, vacancies have combined into a $\frac{1}{2} \langle 111 \rangle$ vacancy dislocation loop (Fig. 8(b)), which is typical for irradiated BCC metals

[87, 88]. Similar behavior was demonstrated earlier, however, only for the V-4Ti alloy, where vacancies remained separated, but at the same time bound into Ti-vV complexes [78].

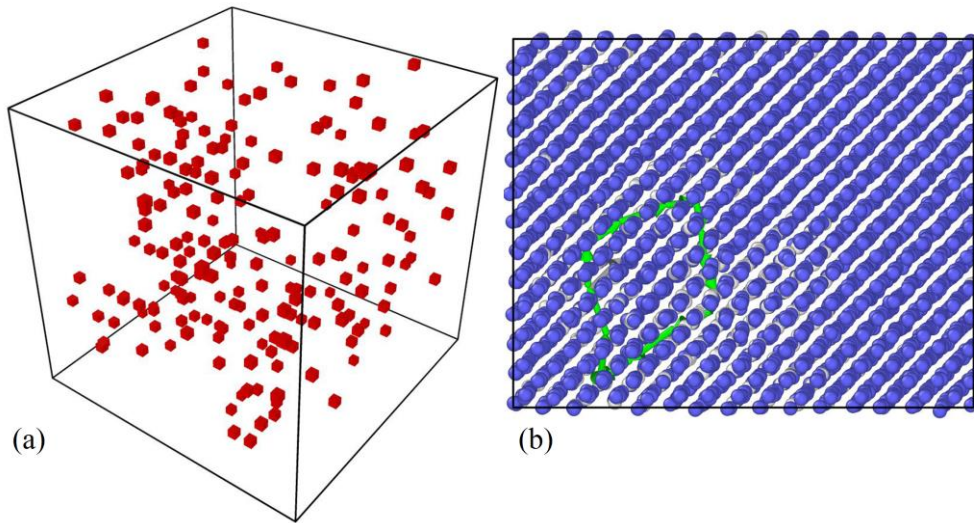


Fig. 8. Results of annealing at 873 K for 15 ns of a vacancy ensemble in the (a) HfNbTiZr alloy and (b) reference Nb.

3.2.3 Migration energy of vacancies and interstitial atoms

The diffusion mobility of interstitial atoms and vacancies is important for understanding the kinetics of cluster nucleation and growth at stages preceding the formation of a defect structure peculiar to a particular material. Figure 9 demonstrates the migration barriers of vacancies (E_v^m) and interstitial atoms (E_i^m) for HfNbTiZr from TAD simulations compared to Nb, as well as for V-4Ti and V (dashdotted lines). As can be seen, most of the E_v^m values for vacancies lie to the left of "vNb (BCC Nb)", while most of the E_i^m values for interstitial atoms lie to the right of "iNb (BCC Nb)". This indicates a decrease in the migration energy of vacancies and its increase for interstitial atoms in the HfNbTiZr alloy compared to the reference Nb (Fig. 9). Namely, from 44 to 65 % of the E_v^m values are lower and from 81 to 92 % of the E_i^m values are higher than in Nb (0.11 and 0.43 eV for an interstitial atom [89] and a vacancy [90], respectively). While an increase in the migration energy for both vacancies (2-fold) and interstitial atoms (6-fold) is inherent for the V-4Ti alloy (Fig. 9) compared to the reference V (0.46 eV for a vacancy and 0.14 eV for an interstitial atom [78]). Thus, an almost full overlap of migration barriers for all types of vacancies and interstitial atoms is typical for the HfNbTiZr alloy, while for the V-4Ti alloy there is a significant closeness of the barriers (Fig. 9). It was also found that the main contribution to diffusion in the HfNbTiZr alloy is driven by Ti and Nb species for both the vacancy and interstitial mechanisms (Fig. 9). The latter is consistent with the lower formation energy of dumbbells based on them (Fig. 6).

It is believed that the lower radiation damage of concentrated alloys compared to pure metals and traditional alloys is due to such factors as: the slow thermal energy dissipation [91-93], the closeness or overlap of migration barriers of vacancies and interstitial atoms [82, 91], the chemically biased diffusion [13, 94, 95]. These factors enhance the defect recombination, change diffusion trajectories and mechanisms [13, 19, 82, 83, 91, 96-98, 99]. The revealed almost full overlap of migration barriers for all types of vacancies and interstitial atoms in HfNbTiZr does not contradict the idea of Ref. [82] regarding the key influence of partially filled *d*-shells on this

overlap due to the electron deformation ability. Thus, all elements in the composition of the HfNbTiZr alloy (Hf: $6s^24f^{14}5d^2$; Nb: $4d^45s^1$; Ti: $3d^24s^2$; Zr: $4d^25s^2$) have less than half-filled d -shells. Thus, the parameters (screening function for the background electron density, *etc.*) for the used MEAM potential with fitting [47] can reproduce a qualitatively correct trend.

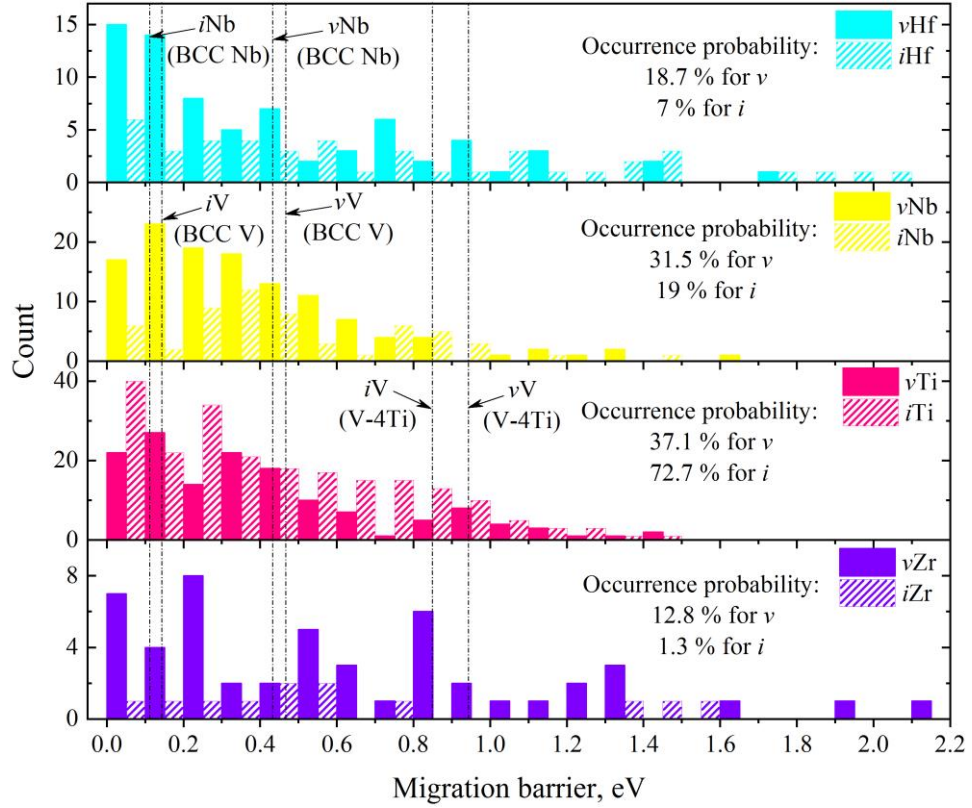


Fig. 9. Migration barriers for vacancies and interstitial atoms in the HfNbTiZr alloy from the TAD simulations. For comparison, the data for the reference Nb [89, 90] and V [78], as well as V-4Ti alloy [78] are given (dashdotted lines).

The decrease and increase of the migration barriers for vacancies and interstitial atoms, respectively, revealed for the HfNbTiZr alloy compared to the reference Nb, is also consistent with the data for other FCC and BCC MCAs [19, 31, 49, 82, 83, 94]. For the NbTiZr alloy, the results of *ab initio* calculations also demonstrated the similarity of E_v^m distributions for all vacancy types, as well as the existence of migration barriers close to 0 eV [31]. The latter was explained by the presence of severe LLD, leading to a significant variation in the energy landscape and suppression of migration barriers between certain lattice sites [31]. In our case, a large difference between the forward and backward vacancy migration energies was also fixed, which could be attributed to the LLD effect [31]. However, the found decrease in the vacancy migration barriers in HfNbTiZr does not indicate a preference growth of large vacancy clusters as compared to Nb due to the preferential migration through low-energy sites [31]. The latter is a manifestation of the sluggish diffusion effect in concentrated alloys, which includes the site percolation and composition constituents [100]. This complements the hindered vacancy clustering described above (Fig. 8), based on the low energy stability of divacancies (Fig. 7).

In the vanadium alloys, oversized solute Ti atoms play the role of effective traps not only for interstitial atoms [78], but also for vacancies [81, 101, 102]. This is the reason for the diffusion suppression of both interstitial atoms and vacancies in the dilute V-4Ti alloy (Fig. 9). In this case,

point defects are stuck in the zones of the Ti- ν V, Ti- i V complexes, thereby increasing the defect recombination rate [78]. The latter should also be proper for the V-4Cr-4Ti alloy.

3.2.4 Binding energy for helium-vacancy complexes and helium diffusion

In general, He bubble nucleation and growth and then bubble swelling are determined by the concurrent processes in which vacancies, interstitial atoms and He atoms are primarily involved (recombination, diffusion, clustering, dissociation, *etc.*) [68]. From this viewpoint, it is important to evaluate the clustering ability of vacancies with He atoms and the He diffusion mobility, which affect the first steps of nascent bubbles in the studied alloys. The results of *ab initio* calculations of He to $\text{He}_{n-1}\nu_m$ and ν to $\text{He}_n\nu_{m-1}$ binding energies on the He/ ν (n/m) ratio for HfNbTiZr and V-4Cr-4Ti are provided in Figure 10. The positive binding energy corresponds to an attractive interaction between defects. It was found that ν to $\text{He}_n\nu_{m-1}$ binding energies are significantly lower in HfNbTiZr than in V-4Cr-4Ti, while He to $\text{He}_{n-1}\nu_m$ binding energies look comparable in both alloys with an increase in the He/ ν ratio (Fig. 10). This leads to the intersection of the fitting curves at a higher He/ ν ratio for HfNbTiZr compared to V-4Cr-4Ti (~ 1.5 versus ~ 1.1 , respectively). Thus, it is suggested that He bubbles are stable at higher He concentrations in HfNbTiZr, unlike V-4Cr-4Ti.

The low binding energies of $\text{He}_n\nu_m$ complexes for HfNbTiZr are consistent with previous atomistic calculations for BCC WTaTi, WTaCrV and WTaCrVTi alloys [103]. In addition, the helium-vacancy binding energy calculations for V-4Cr-4Ti are consistent with previous *ab initio* calculations performed for a simple He ν complex for the same alloy [66]. Note that the low binding energies of $\text{He}_n\nu_m$ complexes in HfNbTiZr may be a consequence of their low formation energies, which is due to the LLD effect, as demonstrated for WTaTi, WTaCrV and WTaCrVTi [103].

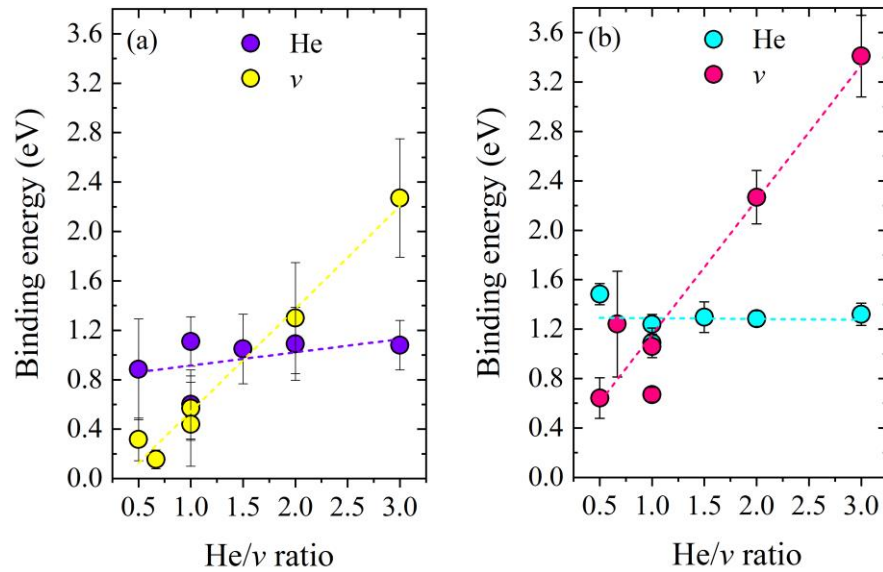


Fig. 10. Binding energies of He to $\text{He}_{n-1}\nu_m$ and ν to $\text{He}_n\nu_{m-1}$ on the He/ ν ratio for (a) HfNbTiZr and (b) V-4Cr-4Ti.

Previous studies of the He behavior in metals have established its high diffusion mobility through tetrahedral sites and low mobility at substitutional sites [68]. The latter is due to the capture of helium with a vacancy because the high binding energy of the He ν complex [68]. To evaluate the highest diffusion mobility of He in the studied alloys, the He diffusion was considered through interstitial sites. Figure 11(a) shows the MSD of He (at 1173 K) averaged over several AIMD trajectories for the HfNbTiZr and V-4Cr-4Ti alloys. The diffusion mobility of He was found to be lower in HfNbTiZr than in V-4Cr-4Ti. For a qualitative understanding of this behavior, Fig. 11(b) depicts the He diffusion trajectories in both alloys. While in V-4Cr-4Ti, solute Ti atoms play the

role of effective traps for He [104], in HfNbTiZr, both Ti and Zr atoms play such a role. In other words, the He atom was stuck for a long time in local Ti- and Zr-rich regions in the HfNbTiZr alloy. This behavior can be explained by the significant positive binding energy for He-Ti and He-Zr pairs, unlike He-Hf and He-Nb pairs [104]. Previous MD simulations also demonstrated a significant suppression of He diffusion in WTaCrV and WTaCrVTi compared to W [103]. However, Ti atoms in the WTaCrVTi and especially in WTaTi alloys played the role of bridges, facilitating and providing long-range He diffusion [103].

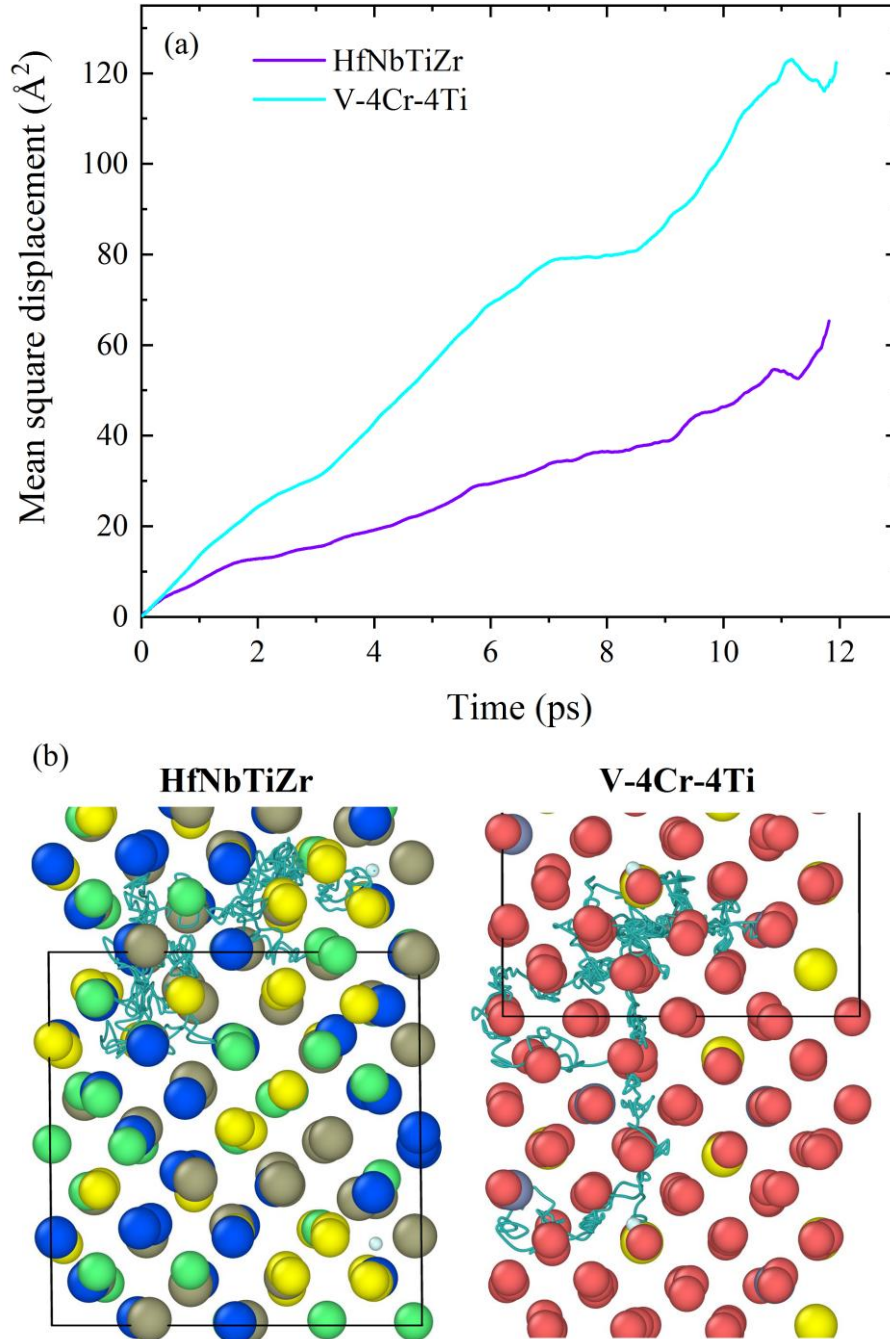


Fig. 11. (a) Mean square displacements and (b) diffusion trajectories of He through the lattice in HfNbTiZr and V-4Cr-4Ti at 1173 K with the same time scale. The gray, light mint, yellow, blue, light coral, glaucous and light cyan balls are used for Hf, Nb, Ti, Zr, V, Cr and He atoms, respectively. The diffusion trajectories are displayed in the unwrap mode.

4. Discussion

Considering that the overall bubble density remains almost constant within the error (Fig. 3(e)), and the peak bubble density decreases (Fig. 3(f)) with increasing fluence in both alloys, at the fluence of $5 \times 10^{17} \text{ cm}^{-2}$, the bubble formation and growth processes still compete with each other on the ion range (overall) scale. In other words, in the peak bubble region, bubble growth occurs due to coalescence rather than absorption of new He atoms and vacancies, while outside this region, new small bubbles form. Thus, it can be said that the decrease in bubble density at the peak is compensated by the appearance of new bubbles outside the peak region, leading to an almost constant overall bubble density. The latter leads to a broader profile of He bubbles along the depth at $5 \times 10^{17} \text{ cm}^{-2}$, which was clearly fixed on the filtered TEM images (see Fig. S5 in the Supplementary Material). Despite the tendency of the He bubble distribution to be homogeneous with increasing fluence in both alloys, HfNbTiZr demonstrates inferior bubble swelling resistance compared to V-4Cr-4Ti.

Taking into account, on the one hand, the almost full overlap of the migration barriers of vacancies and interstitial atoms in the HfNbTiZr alloy, and on the other hand, the closeness of the same barriers in the V-4Ti (V-4Cr-4Ti) alloys (Fig. 9), it can be concluded that the defect recombination efficiencies in the concentrated and dilute alloys are comparable. To support this conclusion, Table 2 lists the numbers of surviving Frenkel pairs after MD simulations of collision cascades initiated by 1 keV PKAs at 300 K in HfNbTiZr and V-4Ti (the accurate potential for the V-Ti solid solutions [61]). The comparability of these data suggests that approximately the same number of irradiation-induced vacancies can be generated in the alloys. The comparability of the Frenkel pair numbers in HfNbTiZr and V-4Ti is consistent with the data on the vacancy and interstitial formation energies (see paragraph 3.2.1). Namely, the sum of $E_v^f + E_i^f$ energies (as the energy of a Frenkel pair formation) gives comparable values in both alloys (4.8 *versus* 4.7 eV for HfNbTiZr and V-4Ti, respectively). In HfNbTiZr, E_v^f is lower and E_i^f is higher, while in V-4Ti (V-4Cr-4Ti), the opposite is valid.

Table 2. Numbers of surviving Frenkel pairs after MD simulations of collision cascades initiated by 1 keV PKAs at 300 K in HfNbTiZr and V-4Ti.

Alloy	Number of Frenkel pairs
HfNbZrTi	8.7±1.9
V-4Ti	9.7±2.2

The low v to $\text{He}_n v_{m-1}$ binding energies found for HfNbTiZr (Fig. 10(a)) mean that additional vacancies are not favorable for the stabilization of helium-vacancy complexes. Based on the binding energy curves, additional He atoms favor the stabilization of the complexes due to the increased He/ v ratio in HfNbTiZr compared to V-4Cr-4Ti (Fig. 10). It is known that the gradual accumulation of He in a helium-vacancy complex induces pressure on the surrounding lattice, which leads to the commonly observed effects of i - v pair formation by kick-out of lattice atoms [68, 105, 106] and dislocation loop punching during the accumulation of interstitial atoms around the He bubble [68, 107, 108, 109]. These are well-known mechanisms of He bubble growth in metals (Kick-Out and Dislocation Loop Punching) [68].

To verify the possibility of implementing the primary kick-out mechanism, we conducted simulations of the evolution for $\text{He}_n v$ complexes in HfNbTiZr and V-4Cr-4Ti using variable-cell

AIMD at 300 K (Fig. 12). The He/ v ratios (9, 11, 13 and 15) were purposely chosen to be the same for both alloys. The selection of high He/ v ratios was based on previous *ab initio* calculations [110], which showed that He $_n$ v complexes with $n \leq 18$ still attract He in vanadium. Figure 12 demonstrates that the kick-out mechanism is triggered earlier both in time and at lower He/ v ratios in HfNbTiZr compared to V-4Cr-4Ti. Namely, in HfNbTiZr, a lattice atom was kicked out by He pressure from the He $_{11}$ v complex (Fig. 12(c)), whereas in V-4Cr-4Ti this was the case for the He $_{15}$ v complex (Fig. 12(h)). At shorter simulation times, interstitial atoms rearranged their configuration in HfNbTiZr, which was not observed in V-4Cr-4Ti even at longer times (Figs. 12(e), 12(f) and 12(g), 12(h)). Besides, in HfNbTiZr, the rearrangement of interstitial atom configurations facilitated their orientation along $\langle 111 \rangle$, which is energetically favorable for the evolution of a prismatic loop [68]. The He/ v ratio decreases when the kick-out mechanism is activated, which stimulates the helium-vacancy complex to capture additional He atoms, thereby contributing to the further He bubble growth [105]. At the same time, the v to He $_n$ v_{m-1} and He to He $_{n-1}$ v_m binding energies on the He/ v ratio change the trend to an opposite in comparison with low He density case [105]. Thus, the kick-out mechanism, preceding the dislocation loop punching mechanism, is enhanced in HfNbTiZr and suppressed in V-4Cr-4Ti.

The kick-out of lattice atoms in HfNbTiZr is accompanied by the formation of dumbbells containing Ti (Fig. 12). This is consistent with their lower formation energy (Fig. 6). We emphasize that Ti and Zr atoms play the role of effective traps for He atoms, thereby retarding their diffusion mobility (Fig. 11(b)). In this regard, to weaken the kick-out mechanism in HfNbTiZr, the concentration of Zr can be increased by decreasing the concentration of Ti. Note that among Hf, Nb, Ti and Zr, Nb atoms have the highest threshold displacement energy [111]. Moreover, Nb exerts a stabilizing effect on the BCC phase [112]. As shown in Ref. [113], Hf negatively affects the phase stability of Hf-Nb-Ti-Zr MCAs, especially at elevated temperatures. In view of the above, in order to enhance the irradiation resistance of HfNbTiZr as a whole, the concentration of Nb can be increased by decreasing the concentration of Hf. Thus, to improve the bubble swelling resistance at low irradiation temperatures, a deviation from the equiatomic composition of HfNbTiZr towards Hf $_{10-15}$ Nb $_{35-40}$ Ti $_{15-20}$ Zr $_{30-35}$ compositions can be proposed. The presented Hf $_{10-15}$ Nb $_{35-40}$ Ti $_{15-20}$ Zr $_{30-35}$ alloy compositions fall within the BCC stability range for solid solution phases based on the valence electron concentration (VEC) parameter or criteria (BCC at VEC < 6.87) [114]: for Hf $_{10-15}$ Nb $_{35-40}$ Ti $_{15-20}$ Zr $_{30-35}$ VEC = 4.35–4.4 (for HfNbTiZr VEC = 4.25 [115]). Nevertheless, further investigations are needed.

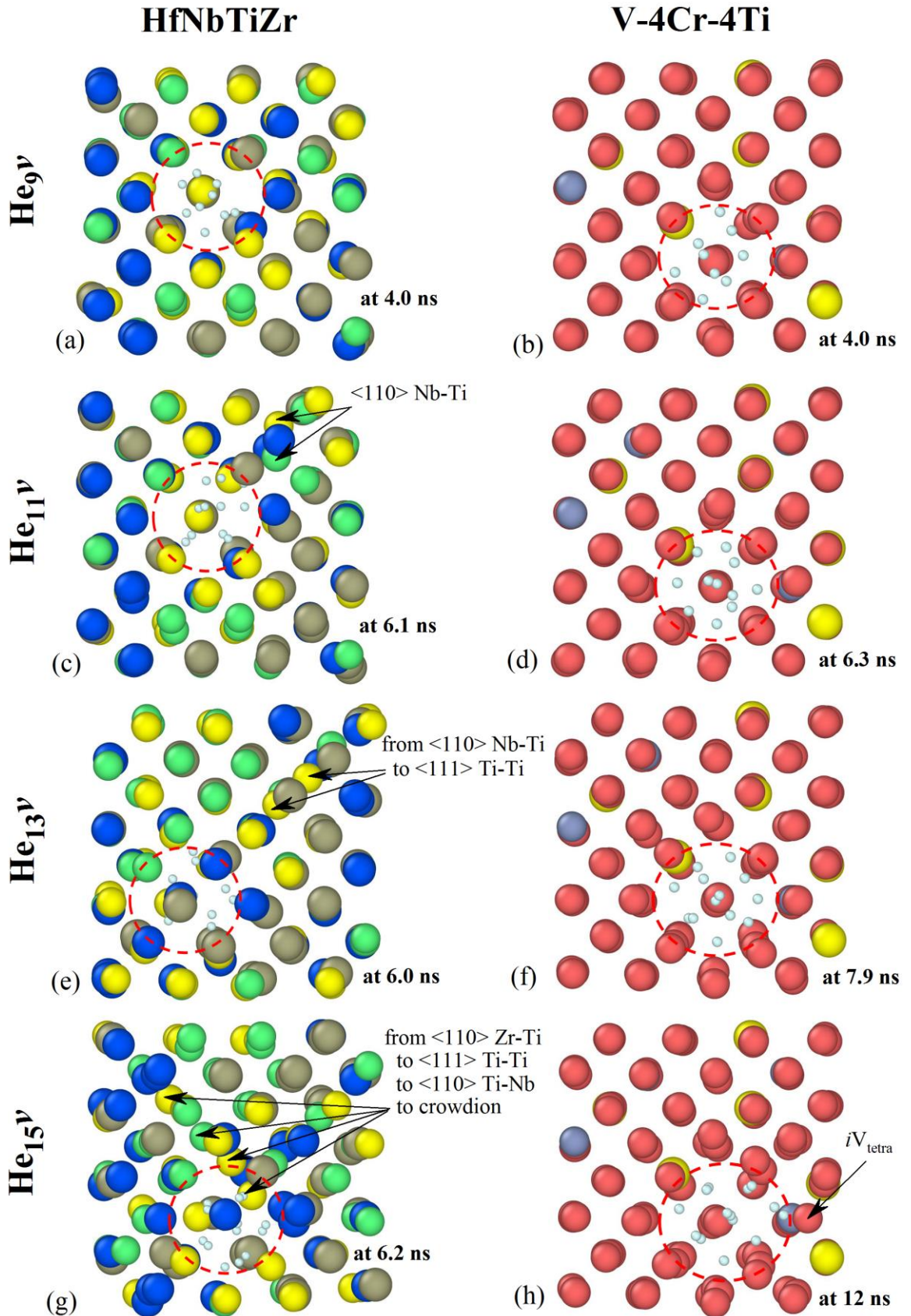


Fig. 12. Variable-cell AIMD simulations of the evolution for $\text{He}_n v$ complexes ($n = 9, 11, 13$ and 15) in the HfNbTiZr and V-4Cr-4Ti alloys at 300 K. The region of complexes is highlighted by a red dashed circle. Snapshots of the structures are shown at the indicated times in (a)-(h). The configurations of interstitial atoms are marked with arrows. The gray, light mint, yellow, blue, light coral, glaucous and light cyan balls are used for Hf, Nb, Ti, Zr, V, Cr and He atoms, respectively.

Conclusions

A comparative study of irradiation resistance for BCC multicomponent concentrated HfNbTiZr and dilute V-4Cr-4Ti alloys, exposed to 40 keV He ions at RT up to fluences of 5×10^{16} , 1×10^{17} and $5 \times 10^{17} \text{ cm}^{-2}$, has been carried out with joint experimental and simulation techniques. Similar to V-4Cr-4Ti, HfNbTiZr exhibits high resistance of the phase composition to irradiation with He ions up to $5 \times 10^{17} \text{ cm}^{-2}$ according to GIXRD. SEM studies for HfNbTiZr showed the absence of blisters and exfoliation at the fluence of $5 \times 10^{17} \text{ cm}^{-2}$, as for V-4Cr-4Ti. Using TEM, higher bubble swelling, as well as its intensification with increasing fluence was found in HfNbTiZr compared to V-4Cr-4Ti. At $5 \times 10^{17} \text{ cm}^{-2}$, the overall swelling (S_{overall}) in HfNbTiZr turned out to be 2 times higher than in V-4Cr-4Ti (0.44 ± 0.05 versus 0.19 ± 0.02 %, respectively). A 5-fold increase in fluence (from 1×10^{17} to $5 \times 10^{17} \text{ cm}^{-2}$) resulted in a 30 % increase in the $S_{\text{overall}}(\text{HfNbTiZr})/S_{\text{overall}}(\text{V-4Cr-4Ti})$ ratio.

Based on the MEAM interatomic potential and DFT, calculations and simulations of the energetics of defects and helium-vacancy complexes, as well as their dynamics for HfNbTiZr and dilute vanadium alloys (V-4Ti, V-4Cr-4Ti) were carried out. Similar to the dilute vanadium alloys, HfNbTiZr is characterized by suppressed vacancy clustering and high defect recombination efficiency. The latter may be a consequence of the almost full overlap of the vacancy and interstitial migration barriers in HfNbTiZr, along with the proximity of these barriers in the dilute vanadium alloys. Herewith, the comparability of the number of Frenkel pairs in the HfNbTiZr and diluted vanadium alloys was shown. In addition, this is consistent with the energetics of Frenkel pair formation in HfNbTiZr and dilute vanadium alloys. Thus, in the HfNbTiZr and dilute vanadium alloys the number of radiation-induced vacancies essential for the nucleation of $\text{He}_{n\nu m}$ complexes can be same. According to the binding energy curves, there is a tendency for higher He accumulation in helium-vacancy complexes due to the increased He/ ν ratio in HfNbTiZr compared to V-4Cr-4Ti (~ 1.5 versus ~ 1.1 , respectively). It was found that the kick-out of lattice atoms is enhanced in HfNbTiZr and is suppressed in V-4Cr-4Ti. Thus, the more intense growth of He bubbles in HfNbTiZr may be due to the kick-out mechanism, which leads to a decrease in the He/ ν ratio and stimulates helium-vacancy complexes to capture additional He atoms.

Acknowledgements

Our work was performed using resources of NRNU MEPhI and NRTPU high-performance computing centers.

Funding

This research was funded by the Science Committee of the Ministry of Science and Higher Education of the Republic of Kazakhstan (Grant No. AP19579188), the Belarusian Republican Foundation for Fundamental Research and Ministry of Education of the Republic of Belarus (Grant No. T22MB-009).

References

- [1] S.J. Zinkle, J.T. Busby, *Mater. Today* **12**(11), 12 (2009). [https://doi.org/10.1016/S1369-7021\(09\)70294-9](https://doi.org/10.1016/S1369-7021(09)70294-9)
- [2] G.S. Was, *Fundamentals of radiation materials science: metals and alloys*, 1-st ed., Springer Berlin, Heidelberg, 2007. <https://doi.org/10.1007/978-3-540-49472-0>
- [3] W. Zhang, P.K. Liaw & Y. Zhang, *Sci. China Mater.* **61**(1), 2 (2018). <https://doi.org/10.1007/s40843-017-9195-8>
- [4] D.B. Miracle, O.N. Senkov, *Acta Mater.* **122**, 448 (2017). <http://dx.doi.org/10.1016/j.actamat.2016.08.081>
- [5] J. Chen, X. Zhou, W. Wang, B. Liu, Y. Lv, W. Yang, D. Xu, Y. Liu, *J. Alloys Compd.* **760**, 15 (2018). <https://doi.org/10.1016/j.jallcom.2018.05.067>
- [6] K. Wang, H. Wang, F. Liu, H. Zhai, *Acta Mater.* **61**(4), 1359 (2013). <https://doi.org/10.1016/j.actamat.2012.11.013>
- [7] K.A. Rozman, M. Detrois, T. Liu, M.C. Gao, P.D. Jablonski, and J.A. Hawk, *JMEP* **29**(9), 5822 (2020). <https://doi.org/10.1007/s11665-020-05103-2>
- [8] M. Sadeghilaridjani, S. Muskeri, M. Pole and S. Mukherjee, *Entropy* **22**(2), 230 (2020). <https://doi.org/10.3390/e22020230>
- [9] Y. Fu, J. Li, H. Luo, C. Du, X. Li, *J. Mater. Sci. Technol.* **80**, 217 (2021). <https://doi.org/10.1016/j.jmst.2020.11.044>
- [10] E. Levo, F. Granberg, C. Fridlund, K. Nordlund, F. Djurabekova, *J. Nucl. Mater.* **490**, 323 (2017). <https://doi.org/10.1016/j.jnucmat.2017.04.023>
- [11] S. Shi, M.-R. He, K. Jin, H. Bei, I.M. Robertson, *J. Nucl. Mater.* **501**, 132 (2018). <https://doi.org/10.1016/j.jnucmat.2018.01.015>
- [12] L. Qian, H. Bao, R. Li and Q. Peng, *Mater. Adv.* **3**, 1680 (2022). <https://doi.org/10.1039/d1ma01184g>
- [13] S. Zhao, Y. Osetsky, Y. Zhang, *Acta Mater.* **128**, 391 (2017). <https://doi.org/10.1016/j.actamat.2017.01.056>
- [14] K. Jin, C. Lu, L.M. Wang, J. Qu, W.J. Weber, Y. Zhang, H. Bei, *Scr. Mater.* **119**, 65 (2016). <http://dx.doi.org/10.1016/j.scriptamat.2016.03.030>
- [15] Y. Zhang, X. Wang, Y.N. Osetsky, Y. Tong, R. Harrison, S.E. Donnelly, D. Chen, Y. Wang, H. Bei, B.C. Sales, K.L. More, P. Xiu, L. Wang, W.J. Weber, *Acta Mater.* **181**, 519 (2019). <https://doi.org/10.1016/j.actamat.2019.10.013>
- [16] C.A. Dennett, B.R. Dacus, C.M. Barr, T. Clark, H. Bei, Y. Zhang, M.P. Short, K. Hattar, *Appl. Mater. Today* **25**, 101187 (2021). <https://doi.org/10.1016/j.apmt.2021.101187>
- [17] O. El-Atwani, N. Li, M. Li, A. Devaraj, J.K.S. Baldwin, M.M. Schneider, D. Sobieraj, J.S. Wróbel, D. Nguyen-Manh, S. A. Maloy, E. Martinez, *Sci. Adv.* **5**(3), eaav2002 (2019). <https://doi.org/10.1126/sciadv.aav2002>
- [18] H. Li, L. Zhao, Y. Yang, H. Zong, X. Ding, *J. Nucl. Mater.* **555**, 153140 (2021). <https://doi.org/10.1016/j.jnucmat.2021.153140>
- [19] J. Byggmästar, K. Nordlund, and F. Djurabekova, *Phys. Rev. B* **104**, 104101 (2021). <https://doi.org/10.1103/PhysRevB.104.104101>
- [20] Y. Zong, N. Hashimoto, H. Oka, *Nucl. Mater. Energy* **31**, 101158 (2022). <https://doi.org/10.1016/j.nme.2022.101158>
- [21] H. Song, F. Tian, Q.-M. Hu, L. Vitos, Y. Wang, J. Shen, and N. Chen, *Phys. Rev. Mater.* **1**, 023404 (2017). <https://doi.org/10.1103/PhysRevMaterials.1.023404>
- [22] Y. Tong, G. Velisa, S. Zhao, W. Guo, T. Yang, K. Jin, C. Lu, H. Bei, J.Y.P. Ko, D.C. Pagan, Y. Zhang, L. Wang, F.X. Zhang, *Materialia* **2**, 73 (2018). <https://doi.org/10.1016/j.mtla.2018.06.008>

- [23] T. Yang, C. Lu, G. Velisa, K. Jin, P. Xiu, Y. Zhang, H. Bei, L. Wang, *Scr. Mater.* **158**, 57 (2019). <https://doi.org/10.1016/j.scriptamat.2018.08.021>
- [24] C. Lu, L. Niu, N. Chen, K. Jin, T. Yang, P. Xiu, Y. Zhang, F. Gao, H. Bei, S. Shi, M.-R. He, I.M. Robertson, W.J. Weber & L. Wang, *Nat. Commun.* **7**, 13564 (2016). <https://doi.org/10.1038/ncomms13564>
- [25] A. Barashev, Y. Osetsky, H. Bei, C. Lu, L. Wang, Y. Zhang, *Curr. Opin. Solid State Mater. Sci.* **23**(2), 92 (2019). <https://doi.org/10.1016/j.cossms.2018.12.001>
- [26] Z. Fan, T. Yang, B. Kombariah, X. Wang, P.D. Edmondson, Y.N. Osetsky, K. Jin, C. Lu, H. Bei, L. Wang, K.L. More, W.J. Weber, Y. Zhang, *Materialia* **9**, 100603 (2020). <https://doi.org/10.1016/j.mtla.2020.100603>
- [27] C. Lu, T. Yang, K. Jin, N. Gao, P. Xiu, Y. Zhang, F. Gao, H. Bei, W.J. Weber, K. Sun, Y. Dong, L. Wang, *Acta Mater.* **127**, 98 (2017). <http://dx.doi.org/10.1016/j.actamat.2017.01.019>
- [28] O.N. Senkov, D.B. Miracle, K.J. Chaput, J.-P. Couzinie, *J. Mater. Res.* **33**, 3092 (2018). <https://doi.org/10.1557/jmr.2018.153>
- [29] Y.D. Wu, Y.H. Cai, T. Wang, J.J. Si, J. Zhu, Y.D. Wang, X.D. Hui, *Mater. Lett.* **130**, 277 (2014). <http://dx.doi.org/10.1016/j.matlet.2014.05.134>
- [30] D. Li, N. Jia, H. Huang, S. Chen, Y. Dou, X. He, W. Yang, Y. Xue, Z. Hua, F. Zhang, L. Wang, K. Jin, H. Cai, *J. Nucl. Mater.* **552**, 153023 (2021). <https://doi.org/10.1016/j.jnucmat.2021.153023>
- [31] T. Shi, Z. Su, J. Li, C. Liu, J. Yang, X. He, D. Yun, Q. Peng, C. Lu, *Acta Mater.* **229**, 117806 (2022). <https://doi.org/10.1016/j.actamat.2022.117806>
- [32] L. Yang, H. Ge, J. Zhang, T. Xiong, Q. Jin, Y. Zhou, X. Shao, B. Zhang, Z. Zhu, S. Zheng, X. Ma, *J. Mater. Sci. Technol.* **35**(3), 300 (2019). <https://doi.org/10.1016/j.jmst.2018.09.050>
- [33] S.J. Zinkle, G.S. Was, *Acta Mater.* **61**, 735 (2013). <http://dx.doi.org/10.1016/j.actamat.2012.11.004>
- [34] M.A. Tunes, H. Le, G. Greaves, C.G. Schön, H. Bei, Y. Zhang, P.D. Edmondson, S.E. Donnelly, *Intermetallics* **110**, 106461 (2019). <https://doi.org/10.1016/j.intermet.2019.04.004>
- [35] N. Jia, Y. Li, H. Huang, S. Chen, D. Li, Y. Dou, X. He, W. Yang, Y. Xue, K. Jin, *J. Nucl. Mater.* **550**, 152937 (2021). <https://doi.org/10.1016/j.jnucmat.2021.152937>
- [36] H.M. Chung, B.A. Loomis, D.L. Smith, *J. Nucl. Mater.* **212-215**, 804 (1994). [https://doi.org/10.1016/0022-3115\(94\)90167-8](https://doi.org/10.1016/0022-3115(94)90167-8)
- [37] D.L. Smith, H.M. Chung, B.A. Loomis, H.-C. Tsai, *J. Nucl. Mater.* **233-237**, 356 (1996). [https://doi.org/10.1016/S0022-3115\(96\)00231-0](https://doi.org/10.1016/S0022-3115(96)00231-0)
- [38] J.F. Ziegler, M.D. Ziegler, and J.P. Biersack, *Nucl. Instrum. Methods Phys. Res. B* **268**, 1818 (2010). <https://doi.org/10.1016/j.nimb.2010.02.091>
- [39] G.W. Egeland, J.A. Valdez, S.A. Maloy, K.J. McClellan, K.E. Sickafus, G.M. Bond, *J. Nucl. Mater.* **435**, 77 (2013). <https://doi.org/10.1016/j.jnucmat.2012.12.025>
- [40] P. Colombi, P. Zanola, E. Bontempi, R. Roberti, M. Gelfi, L.E. Depero, *J. Appl. Crystallogr.* **39**(2), 176 (2006). <https://doi.org/10.1107/s0021889805042779>
- [41] C.A. Schneider, W.S. Rasband, & K.W. Eliceiri, *Nat. Methods* **9**(7), 671 (2012). <https://doi.org/10.1038/nmeth.2089>
- [42] D. Legland, I. Arganda-Carreras, & P. Andrey, *Bioinform.* **32**(22), 3532 (2016). <https://doi.org/10.1093/bioinformatics/btw413>
- [43] A.R. Oganov and C.W. Glass, *J. Chem. Phys.* **124**, 244704 (2006). <https://doi.org/10.1063/1.2210932>
- [44] A.O. Lyakhov, A.R. Oganov, H.T. Stokes, and Q. Zhu, *Comp. Phys. Comm.* **184**, 1172 (2013). <https://doi.org/10.1016/j.cpc.2012.12.009>
- [45] A.R. Oganov, A.O. Lyakhov, and M. Valle, *Acc. Chem. Res.* **44**(3), 227 (2011). <https://doi.org/10.1021/ar1001318>
- [46] S. Plimpton, *J. Comp. Phys.* **117**, 1 (1995). <https://doi.org/10.1006/jcph.1995.1039>

- [47] X. Huang, L. Liu, X. Duan, W. Liao, J. Huang, H. Sun, C. Yu, *Mater. Des.* **202**, 109560 (2021). <https://doi.org/10.1016/j.matdes.2021.109560>
- [48] D. Nguyen-Manh, A. P. Horsfield, and S. L. Dudarev, *Phys. Rev. B* **73**, 020101(R) (2006). <https://doi.org/10.1103/PhysRevB.73.020101>
- [49] S. Zhao, G.M. Stocks and Y. Zhang, *Phys. Chem. Chem. Phys.* **18**, 24043 (2016). <https://doi.org/10.1039/c6cp05161h>
- [50] M.R. Sorensen and A.F. Voter, *J. Chem. Phys.* **112**, 9599 (2000). <https://doi.org/10.1063/1.481576>
- [51] G. Henkelman, B.P. Uberuaga, H. Jonsson, *J. Chem. Phys.* **113**, 9901 (2000). <https://doi.org/10.1063/1.1329672>
- [52] S.B. Maisel, W.-S. Ko, J.-L. Zhang, B. Grabowski, and J. Neugebauer, *Phys. Rev. Materials* **1**, 033610 (2017). <https://doi.org/10.1103/PhysRevMaterials.1.033610>
- [53] J. F. Ziegler, J. P. Biersack, U. Littmark, *The Stopping and Range of Ions in Matter*, Pergamon, New York, 1985.
- [54] P. Giannozzi et al., *J. Phys.: Condens. Matter* **21**, 395502 (2009). <https://doi.org/10.1088/0953-8984/21/39/395502>
- [55] P. Giannozzi et al., *J. Phys.: Condens. Matter* **29**, 465901 (2017). <https://doi.org/10.1088/1361-648X/aa8f79>
- [56] P. Giannozzi et al., *J. Chem. Phys.* **152**, 154105 (2020). <https://doi.org/10.1063/5.0005082>
- [57] J.P. Perdew, K. Burke, M. Ernzerhof, *Phys. Rev. Lett.* **77**, 3865 (1996). <https://doi.org/10.1103/PhysRevLett.77.3865>
- [58] P.E. Blöchl, *Phys. Rev. B* **50**, 17953 (1994). <https://doi.org/10.1103/PhysRevB.50.17953>
- [59] G. Kresse, D. Joubert, *Phys. Rev. B* **59**, 1758 (1999). <https://doi.org/10.1103/PhysRevB.59.1758>
- [60] P. Zhang, T. Zou, J. Zhao, *J. Nucl. Mater.* **467**, 465 (2015). <https://doi.org/10.1016/j.jnucmat.2015.09.039>
- [61] N. Marzari, D. Vanderbilt, A.D. Vita, and M.C. Payne, *Phys. Rev. Lett.* **82**, 3296 (1999). <https://doi.org/10.1103/PhysRevLett.82.3296>
- [62] H.J. Monkhorst, J.D. Pack, *Phys. Rev. B* **13**, 5188 (1976). <https://doi.org/10.1103/PhysRevB.13.5188>
- [63] P. Hirel, *Comput. Phys. Comm.* **197**, 212 (2015). <https://doi.org/10.1016/j.cpc.2015.07.012>
- [64] P. Zhang, J. Zhao, Y. Qin, B. Wen, *J. Nucl. Mater.* **419**, 1 (2011). <https://doi.org/10.1016/j.jnucmat.2011.08.023>
- [65] W. Unn-Toc, M.-C. Marinica, T. Jourdan, *Comput. Mater. Sci.* **145**, 197 (2018). <https://doi.org/10.1016/j.commatsci.2017.12.011>
- [66] P. Zhang, J. Zhao, Y. Qin, B. Wen, *J. Nucl. Mater.* **413**, 90 (2011). <https://doi.org/10.1016/j.jnucmat.2011.03.031>
- [67] J. Ding, P. Zhang, D. Sun, Y. Wang, S. Huang, J. Zhao, *J. Nucl. Mater.* **513**, 143 (2019). <https://doi.org/10.1016/j.jnucmat.2018.10.031>
- [68] S.-H. Li, J.-T. Li and W.-Z. Han, *Materials* **12**, 1036 (2019). <https://doi.org/10.3390/ma12071036>
- [69] Y.-X. Zhai, Y.-H. Li, T.-R. Yang, S. Zhao, F. Tian, L.-M. Liu, H.-B. Zhou, G.-H. Lu, *Scr. Mater.* **242**, 115930 (2024). <https://doi.org/10.1016/j.scriptamat.2023.115930>
- [70] M. Levesque, meanSquaredDisplacement Code, <https://github.com/maxlevesque/meanSquaredDisplacement>, 2024 (accessed 3 July 2024).
- [71] A. Stukowski, *Modelling Simul. Mater. Sci. Eng.* **18**, 015012 (2009). <https://doi.org/10.1088/0965-0393/18/1/015012>
- [72] I.I. Chernov, M.S. Staltsov, B.A. Kalin, O.S. Mezina, Kyi Zin Oo, and V.M. Chernov, *At. Energy* **109**(3), 176 (2011). <https://doi.org/10.1007/s10512-011-9341-4>

- [73] K. Fukumoto, H. Matsui, M. Narui, M. Yamazaki, *J. Nucl. Mater.* **437**, 341 (2013). <http://dx.doi.org/10.1016/j.jnucmat.2013.02.012>
- [74] S.N. Jiang, L.Q. Xu, P.F. Zheng, *Nucl. Mater. Energy* **16**, 19 (2018). <https://doi.org/10.1016/j.nme.2018.06.008>
- [75] X. Zhang, K. Hattar, Y. Chen, L. Shao, J. Li, C. Sun, K. Yu, N. Li, M.L. Taheri, H. Wang, J. Wang, M. Nastasi, *Prog. Mater. Sci.* **96**, 217 (2018). <https://doi.org/10.1016/j.pmatsci.2018.03.002>
- [76] G.F. Vander Voort (Ed.), *ASM Handbook, Vol. 9: Metallography and Microstructures*, ASM International, 2004. <https://doi.org/10.31399/asm.hb.v09.9781627081771>
- [77] J. Fu, X. Li, B. Johansson, J. Zhao, *J. Alloys Compd.* **705**, 369 (2017). <https://doi.org/10.1016/j.jallcom.2017.02.103>
- [78] A.O. Boev, I.V. Nelasov, A.G. Lipnitskii, A.I. Kartamyshev, D.A. Aksyonov, *Solid State Commun.* **329**, 114252 (2021). <https://doi.org/10.1016/j.ssc.2021.114252>
- [79] P. Zhang, Y. Li, J. Zhao, *J. Nucl. Mater.* **538**, 152253 (2020). <https://doi.org/10.1016/j.jnucmat.2020.152253>
- [80] P.-W. Ma and S.L. Dudarev, *Phys. Rev. Mater.* **3**, 013605 (2019). <https://doi.org/10.1103/PhysRevMaterials.3.013605>
- [81] A.O. Boev, D.A. Aksyonov, A.I. Kartamyshev, V.N. Maksimenko, I.V. Nelasov, A.G. Lipnitskii, *J. Nucl. Mater.* **492**, 14 (2017). <http://dx.doi.org/10.1016/j.jnucmat.2017.04.046>
- [82] S. Zhao, T. Egami, G.M. Stocks, Y. Zhang, *Phys. Rev. Mater.* **2**, 013602 (2018). <https://doi.org/10.1103/PhysRevMaterials.2.013602>
- [83] S. Zhao, *J. Mater. Sci. Technol.* **44**, 133 (2020). <https://doi.org/10.1016/j.jmst.2019.10.025>
- [84] M.R. Fellingner, H. Park, and J.W. Wilkins, *Phys. Rev. B* **81**, 144119 (2010). <http://dx.doi.org/10.1103/PhysRevB.81.144119>
- [85] P. Brommer, L.K. Beland, J.-F. Joly, N. Mousseau, *Phys. Rev. B* **90**, 134109 (2014). <https://doi.org/10.1103/PhysRevB.90.134109>
- [86] Y. Fan, A. Kushima, S. Yip, B. Yildiz, *Phys. Rev. Lett.* **106**, 125501 (2011). <https://doi.org/10.1103/PhysRevLett.106.125501>
- [87] C.A. English, *J. Nucl. Mater.* **108 & 109**, 104 (1982). [https://doi.org/10.1016/0022-3115\(82\)90477-9](https://doi.org/10.1016/0022-3115(82)90477-9)
- [88] C.C. Matthai and D.J. Bacon, *J. Nucl. Mater.* **125**, 138 (1984). [https://doi.org/10.1016/0022-3115\(84\)90541-5](https://doi.org/10.1016/0022-3115(84)90541-5)
- [89] S. Bukkuru, U. Bhardwaj, K.S. Rao, A.D.P. Rao, M. Warriar and M.C. Valsakumar, *Mater. Res. Express* **5**, 035513 (2018). <https://doi.org/10.1088/2053-1591/aab418>
- [90] S. Shang, B. Zhou, W.Y. Wang, A.J. Ross, X.L. Liu, Y. Hu, H. Fang, Y. Wang, Z. Liu, *Acta Mater.* **109**, 128 (2016). <http://dx.doi.org/10.1016/j.actamat.2016.02.031>
- [91] Y. Zhang, S. Zhao, W.J. Weber, K. Nordlund, F. Granberg, and F. Djurabekova, *Curr. Opin. Solid State Mater. Sci.* **21**, 221 (2017). <https://doi.org/10.1016/j.cossms.2017.02.002>
- [92] Y. Zhang, G.M. Stocks, K. Jin, C. Lu, H. Bei, B.C. Sales, L. Wang, L.K. Béland, R.E. Stoller, G.D. Samolyuk, M. Caro, A. Caro & W.J. Weber, *Nat. Commun.* **6**, 8736 (2015). <http://dx.doi.org/10.1038/ncomms9736>
- [93] M.W. Ullah, D.S. Aidhy, Y. Zhang, W.J. Weber, *Acta Mater.* **109**, 17 (2016). <https://doi.org/10.1016/j.actamat.2016.02.048>
- [94] Y.N. Osetsky, L.K. Béland, R.E. Stoller, *Acta Mater.* **115**, 364 (2016). <https://doi.org/10.1016/j.actamat.2016.06.018>
- [95] L. Barnard, D. Morgan, *J. Nucl. Mater.* **449**, 225 (2014). <https://doi.org/10.1016/j.jnucmat.2013.10.022>
- [96] H.-S. Do, B.-J. Lee, *Sci. Rep.* **8**, 16015 (2018). <https://doi.org/10.1038/s41598-018-34486-5>

- [97] Y. Lin, T. Yang, L. Lang, C. Shan, H. Deng, W. Hu, F. Gao, *Acta Mater.* **196**, 133 (2020). <https://doi.org/10.1016/j.actamat.2020.06.027>
- [98] G. Veliş, E. Wendler, S. Zhao, K. Jin, H. Bei, W.J. Weber & Y. Zhang, *Mater. Res. Lett.* **6**(2), 136 (2018). <https://doi.org/10.1080/21663831.2017.1410863>
- [99] Y. Li, R. Li, Q. Peng and S. Ogata, *Nanotechnology* **31**, 425701 (2020). <https://doi.org/10.1088/1361-6528/ab9cf5>
- [100] Y.N. Osetsky, L.K. Béland, A.V. Barashev, Y. Zhang, *Curr. Opin. Solid State Mater. Sci.* **22**(3), 65 (2018). <https://doi.org/10.1016/j.cossms.2018.05.003>
- [101] H. Matsui, K. Kuji, M. Hasegawa, A. Kimura, *J. Nucl. Mater.* **212-215**, 784 (1994). [https://doi.org/10.1016/0022-3115\(94\)90163-5](https://doi.org/10.1016/0022-3115(94)90163-5)
- [102] K. Fukumoto, A. Kimura, H. Matsui, *J. Nucl. Mater.* **258-263**, 1431 (1998). [https://doi.org/10.1016/S0022-3115\(98\)00324-9](https://doi.org/10.1016/S0022-3115(98)00324-9)
- [103] Y. Xiong, K. Wang, S. Zhao, *J. Nucl. Mater.* **595**, 155060 (2024). <https://doi.org/10.1016/j.jnucmat.2024.155060>
- [104] P. Zhang, X. Wang, M. Wei, Y. Wang, T. Zou, *Nucl. Mater. Energy* **31**, 101189 (2022). <https://doi.org/10.1016/j.nme.2022.101189>
- [105] K. Morishita, R. Sugano, B.D. Wirth, *J. Nucl. Mater.* **323**, 243 (2003). <https://doi.org/10.1016/j.jnucmat.2003.08.019>
- [106] L. Sandoval, D. Perez, B.P. Uberuaga, A.F. Voter, *Acta Mater.* **159**, 46 (2018). <https://doi.org/10.1016/j.actamat.2018.07.075>
- [107] H. Trinkaus, W.G. Wolfer, *J. Nucl. Mater.* **122**, 552 (1984). [https://doi.org/10.1016/0022-3115\(84\)90655-X](https://doi.org/10.1016/0022-3115(84)90655-X)
- [108] L. Sandoval, D. Perez, B.P. Uberuaga, A.F. Voter, *Phys. Rev. Lett.* **114**, 105502 (2015). <http://dx.doi.org/10.1103/PhysRevLett.114.105502>
- [109] H.X. Xie, N. Gao, K. Xu, G.H. Lu, T. Yu, F.X. Yin, *Acta Mater.* **141**, 10 (2017). <https://doi.org/10.1016/j.actamat.2017.09.005>
- [110] R. Li, P. Zhang, C. Zhang, X. Huang, J. Zhao, *J. Nucl. Mater.* **440**, 557 (2013). <https://doi.org/10.1016/J.jnucmat.2013.03.068>
- [111] A.Yu. Konobeyev, U. Fischer, Yu.A. Korovin, S.P. Simakov, *NUCET* **3**, 169 (2017). <https://doi.org/10.1016/j.nucet.2017.08.007>
- [112] J.H. Dai, W. Li, Y. Song, L. Vitos, *Mater. Des.* **182**, 108033 (2019). <https://doi.org/10.1016/j.matdes.2019.108033>
- [113] T. Li, S. Wang, W. Fan, Y. Lu, T. Wang, T. Li, P.K. Liaw, *Acta Mater.* **246**, 118728 (2023). <https://doi.org/10.1016/j.actamat.2023.118728>
- [114] S. Guo, C. Ng, J. Lu, and C.T. Liu, *J. Appl. Phys.* **109**, 103505 (2011). <https://doi.org/10.1063/1.3587228>
- [115] Wang, W.Y., Shang, S.L., Wang, Y. et al., *npj Comput. Mater.* **3**, 23 (2017). <https://doi.org/10.1038/s41524-017-0024-0>